AD A078056

DDC FILE COPY

(18) AFOSR-TR- 79-1235

(9) SEMI-ANNUAL TECHNICAL REPORT.
1 Oct 1978 — 31 March 1979,

(8) LEVEL II

ARPA Order No.:	3291, Amendment 11
Program Code:	8F10
Name of Contractor:	California Institute of Technology
Effective Date of Contract:	1 October 1976
Contract Expiration Date:	30 September 1979
Amount of Contract:	$407,063
Contract Number:	F49620-77-C-0022
Principal Investigators and Telephone Numbers:	(10) David G. Harkrider, (213) 795-6811, Ext. 2910 Donald V. Helmberger (213) 795-6811, Ext. 2911 J. Bernard Minster (213) 795-6811, Ext. 2909
Program Manager and Telephone Number:	William J. Best (202) 767-5011
Short Title of Work:	(6) Body and Surface Wave Modeling of Observed Seismic Events,

(19) TR-79-1235

(11) Sep 79

(12) 196

DDC RECEIVED DEC 12 1979 A

The views and conclusions contained in this document are those of the authors and should not be interpreted as necessarily representing the official policies, either expressed or implied, of the Defense Advanced Research Projects Agency or the U. S. Government.

Sponsored by
Advanced Research Projects Agency (DOD)
ARPA Order No. 3291, Amendment 11
Monitored by AFOSR Under Contract F49620-77-C-0022,
(15) ARPA Order-3291

Seismological Laboratory
Division of Geological and Planetary Sciences
California Institute of Technology
Pasadena, California 91125

79 12 10 082

320050 gm

Approved for public release; distribution unlimited.

UNCLASSIFIED

SECURITY CLASSIFICATION OF THIS PAGE (When Data Entered)

REPORT DOCUMENTATION PAGE	READ INSTRUCTIONS BEFORE COMPLETING FORM
1. REPORT NUMBER **AFOSR-TR- 79 - 1235** / 2. GOVT ACCESSION NO.	3. RECIPIENT'S CATALOG NUMBER
4. TITLE (and Subtitle) Body and Surface Wave Modeling of Observed Seismic Events	5. TYPE OF REPORT & PERIOD COVERED Semi-annual Technical Report 1 Oct. 1978 - 31 March 1979
	6. PERFORMING ORG. REPORT NUMBER
7. AUTHOR(s) David G. Harkrider Donald V. Helmberger J. Bernard Minster	8. CONTRACT OR GRANT NUMBER(s) F49620-77-C-0022
9. PERFORMING ORGANIZATION NAME AND ADDRESS California Institute of Technology Seismological Laboratory Pasadena, California 91125	10. PROGRAM ELEMENT, PROJECT, TASK AREA & WORK UNIT NUMBERS ARPA Order 3291, Amendmt. 11 8F10
11. CONTROLLING OFFICE NAME AND ADDRESS ARPA/NMR 1400 Wilson Blvd Arlington VA 22209	12. REPORT DATE September 1979 13. NUMBER OF PAGES 60
14. MONITORING AGENCY NAME & ADDRESS (if different from Controlling Office) AFOSR/NP Bolling AFB Wash DC 20332	15. SECURITY CLASS. (of this report) Unclassified 15a. DECLASSIFICATION/DOWNGRADING SCHEDULE

16. DISTRIBUTION STATEMENT (of this Report)

Approved for public release; distribution unlimited

17. DISTRIBUTION STATEMENT (of the abstract entered in Block 20, if different from Report)

18. SUPPLEMENTARY NOTES

19. KEY WORDS (Continue on reverse side if necessary and identify by block number)

Upper mantle structure
Scattering
Wave propagation
Shear wave generation from block movements

20. ABSTRACT (Continue on reverse side if necessary and identify by block number)

The research performed under this contract during the period 1 Oct. 1978 through 31 March 1979 can be divided into three main topics, upper mantle studies, propagational distortions caused by non-planar structure and S wave generation by block movements near explosions.

In Section ~~II~~ 2, we discuss the upper mantle structure of northwestern Eurasia where long period and short period WWSS seismograms from nuclear explosions in the Soviet Union have been incorporated with published apparent velocity data

Cont'd

DD FORM 1 JAN 73 1473

UNCLASSIFIED

Unclassified

to derive a compressional wave velocity model for the upper mantle beneath northwest Eurasia. The waveforms were modeled using generalized ray theory and a starting model was perturbed by trial and error until a fit was achieved. The seismograms from 9-13° exhibit impulsive first arrivals (P_n), implying a smooth, positive velocity gradient between depths of 60 and 150 km. A consistent pulse arriving about 2 seconds after P_n at the ranges 11 to 17° is modeled by positioning a low velocity zone between 150 and 200 km. The P_n phase becomes diffracted beyond 15° although there is considerable evidence of lateral variation at where this geometric cut-off occurs. The model is relatively smooth from a depth of 200 km down to 420 km where a 5% jump in velocity produces a triplication from 15 to 23°. The observations from 21 to 26° clearly show another discontinuity at a depth of 675 km with a 4% change in velocity

In Section 3, glorified optics has been used to compare the waveform complications caused by two and three dimensional structures. A scheme is developed to synthesize seismic images, in which the direct rays give a preliminary feature of a structure, while the multiple boundes provide further information for improving and refining the model. A method is discussed for inverting non-stratified structures like sedimentary basins and subduction plates.

In Section 4, we consider the problem of reflection and refraction of purely compressional waves incident on an interface separating identical solid half-spaces in which the condition of continuity of shear displacement at the boundary is generalized to one that allows slippage. The problem is solved using the Cagniard-de Hoop technique. It is found that the generation of reflected P and S waves, as well as transmitted S waves, is most effective in the case of a perfectly unbounded half-space. We discuss the implications of this model for the generation of S waves by block movement in the vicinity of an underground explosion.

69 12 10 082

TABLE OF CONTENTS

		Page
I.	Summary	1-2
II.	Upper Mantle Structure of Northwestern Eurasia	
III.	Teleseismic Prospecting of Non-stratified Receiver Structure	
IV.	Slipping Interfaces, a Possible Source of S Radiation from Explosive Sources.	

Accession For
NTIS GRA&I
DDC TAB
Unannounced
Justification
By
Distribution/
Availability Codes
Dist | Avail and/or special
A

AIR FORCE OFFICE OF SCIENTIFIC RESEARCH (AFSC)
NOTICE OF TRANSMITTAL TO DDC
This technical report has been reviewed and is approved for public release IAW AFR 190-12 (7b).
Distribution is unlimited.
A. D. BLOSE
Technical Information Officer

I. SUMMARY

The research performed under this contract during the period 1 October 1978 through 31 March 1979 can be divided into three main topics, upper mantle studies, propagational distortions caused by non-planar structure and S-wave generation by block movements near explosions.

In Section II, we discuss the upper mantle structure of northwestern Eurasia where long- and short-period WWSS seismograms from nuclear explosions in the Soviet Union have been incorporated with published apparent velocity data to derive a compressional wave velocity model for the upper mantle beneath northwest Eurasia. The waveforms were modeled using generalized ray theory and a starting model was perturbed by trial and error until a fit was achieved. The seismograms from 9 to 13° exhibit impulsive first arrivals (P_n), implying a smooth, positive velocity gradient between depths of 60 and 150 km. A consistent pulse arriving about 2 seconds after P_n at the ranges 11 to 17° is modeled by positioning a low velocity zone between 150 and 200 km. The P_n phase becomes diffracted beyond 15° although there is considerable evidence of lateral variation at where this geometric cut-off occurs. The model is relatively smooth from a depth of 200 km down to 420 km where a 5% jump in velocity produces a triplication from 15 to 23°. The observations from 21 to 26° clearly show another discontinuity at a depth of 675 km with a 4% change in velocity.

In Section III, glorified optics has been used to compare the waveform complications caused by two and three dimensional structures.

A scheme is developed to synthesize seismic images, in which the direct rays give a preliminary feature of a structure, while the multiple bounces provide further information fir improving and refining the model. A method is discussed for inverting non-stratified structures like sedimentary basins and subduction plates.

In Section IV, we consider the problem of reflection and refraction of purely compressional waves incident on an interface separating identical solid half-spaces in which the condition of continuity of shear displacement at the boundary is generalized to one that allows slippage. The problem is solved using the Cagniard-de Hoop technique. It is found that the generation of reflected P and S waves, as well as transmitted S waves, is most effective in the case of a perfectly unbounded half-space. We discuss the implications of this model for the generation of S waves by block movement in the vicinity of an underground explosion.

II. UPPER MANTLE STRUCTURE OF NORTHWESTERN EURASIA

J. W. Given and D. V. Helmberger

I. INTRODUCTION

There is considerable interest in structure of the upper mantle with respect to the current problems in geodynamics. Although there seems to be broad agreement on the major structural features of the mantle, the various models proposed vary significantly in detail. Important questions yet to be resolved are: (1) how deep are the so-called "400" and "600" km discontinuities; (2) how large are the velocity jumps; (3) how deep in the mantle do velocity variations exist; and (4) how well do these variations correlate with other plate properties.

To answer these difficult seismological questions requires more model resolution than generally provided by the classical methods, namely travel times and a sparse set of ($dT/d\Delta$) measurements, see Wiggins [1969]. Some of the ambiguity of earth models determined by classical means can be eliminated by the use of short-period synthetic seismograms. Comparing the relative amplitudes of observed short-period multiple arrivals to synthetics allows a better determination of triplication points as discussed by Helmberger and Wiggins [1971]. Several regionalized models for the western North American continent have been obtained using this approach, see Wiggins and Helmberger [1973] and Dey-Sarker and Wiggins [1976]. Unfortunately, short-period seismograms suffer from waveform instability in that neighboring stations in many situations do not produce similar pulses. On the other hand, long-period body wave studies indicate that waveshapes recorded on the long-period World-Wide Standard Seismograph Network (WWSSN) are remarkably coherent, see Burdick and Helmberger [1978] and Helmberger and Burdick [1979]. Thus, an acceptable model must yield synthetics which agree with the observed travel times, the $dT/d\Delta$ measurements, the relative timing and amplitudes of short-period pulses, and the long-

period waveshapes. Accurate determinations of the earth's Green's functions, or the broad-band step responses used in this synthetic modeling, for various regions would be very useful in quantitatively answering the questions posed above. To this end, a data-set compiled from Soviet explosions was used to obtain an upper-mantle model which will be used as a reference model in comparing other regions.

There have been a relatively large number of nuclear explosions in western Russia since the deployment of the WWSSN. Many of these events were well recorded in northern Europe at triplication ranges, see Fig. 1. One particularly appealing feature of this data set is the apparent absence of a shadow zone near 9° that is common in regions of western United States, see Romney et al. [1962] and Helmberger [1973b]. A typical seismogram at 9° produced by a N.Z. event is displayed in Fig. 2. Note the sharp P and S phases with little signs of any differential attenuation. This feature is most easily explained by restricting the propagation path to be entirely in the lithosphere. Thus, we have the prospect of determining a complete model whereas in previous studies, the serious nonuniqueness caused by the low velocity zone, (LVZ) made the absolute depths of the upper mantle discontinuities difficult to resolve.

In addition, the NORSAR array is favorably located to measure the apparent velocity of the different phases in the P-wavetrain, and, thus, measure $(dT/d\Delta)$. Several recent investigators, King and Calcagnite [1976], Masse and Alexander [1974], and others, have used these measurements to study the upper mantle. We incorporated their apparent velocity information into our study by adopting KCA, the model proposed by King and Calcagnile [1976], as our starting model. The initial model was modified as required by the waveform data but the $dT/d\Delta$ curve was perturbed as little as possible.

II. SYNTHETIC SEISMOGRAMS FOR EXPLOSIVE SOURCES

The computational procedure used in generating synthetics is well established, namely one assumes that a synthetic can be represented by a series of linear operators:

$$y(t) = s(t)*m\ (t)*\ a(t)*\ r(t)*\ i(t).$$

s(t) represents the source; m(t), the mantle response; a(t) an attenuation operator; r(t) isthe receiver structure; and i(t) is the instrument.

We calculate the source time function by the procedure discussed in Burdick and Helmberger [1979]. The time function parameterization is taken from Von Seggern and Blandford [1972]. The far-field time function is written

$$s(t) = \psi_o \frac{d}{dt} \{1-e^{-kt}\ (1+kt-B(kt)^2\} H(t)*\ C(t)$$

where ψ_o is an amplitude factor, C(t) is an operator representing the effects of the free surface, and B and k are adjustable parameters controlling the shape of the time function.

The parameter B controls the tradeoff between an impulsive and step-like time function. A larger value of B means that the source is more step-like, a smaller value of B indicates a more impulsive time function. In larger nuclear explosions (i.e., for modeling long-period seismograms) we found that B = 6 was an appropriate value to adequately reproduce the teleseismic observations. For smaller explosions and short-period seismograms a value of B = 2 was found to be suitable.

The parameter k is used to adjust pulse width and rise time. Larger explosions are modeled by assuming k = 3, small explosions are modeled by taking k = 5.

The parameters B and k trade off with the operator C(t) which models the effects of the free surface. The shallow source depth causes the negative reflection from the free surface to filter out the low frequencies in the timefunction mimicking the effect of both B and k. We found that P-pP delays of 0.9 sec for large events and 0.6 sec for small events were appropriate for our purposes. The reflection coefficient at the free surface was taken to be -0.8. As we calculate synthetics for different ranges, the trade off angle of P and pP change. As a result the pP-P delay and the free surface reflection coefficient vary with the distance to the receiver. We have found that the change in take-off angle has a small effect on the waveforms, not significant in view of the other uncertainties in the source operator. The operator C(t) also includes the crustal response at the source. Anomalously large S waves (as in Fig. 2), observable out to 15° suggest that there may be some crustal contamination in sources at Novaya Zemlya. We could find no evidence in the long-period P waves for any large distortion due to source structure so the effect has been ignored. In short-period seismograms source structure is important and causes a significant amount of noise which is difficult to interpret. However an uncertainty has been introduced which should be considered in the interpretation.

At ranges where the arrivals from the upper mantle are separated in time, the uncertainties due to the source function are minimal. At ranges where the arrivals from the upper mantle interfere, the errors in the source function can strongly affect the synthetics. Of particular difficulty are secondary p-wave arrivals which interfere with the second upswing of the first arrival. We tested the different sources to check the validity of our conclusions in these situations.

The effect of anelasticity are approximated by a Futterman attenuation

operator [Futterman, 1962; Carpenter, 1966] with T/Q = 1 for all ranges. Kennett [1975] has pointed out the errors introduced by this approximation when low Q zones are present in the upper mantle. The assumption was reevaluated by Burdick and Helmberger [1978] and they concluded that the relative amplitudes (waveforms) were not affected significantly. We do not have a data set which can be used to constrain Q so we will follow the technique used by Burdick and Helmberger [1978].

The receiver operator models the effect of locating the receiver on the free surface and the effect of crustal structure beneath the receiver. The scale of the inhomogeneities in the crust are often small enough to be ignored on the long-period seismograms, see Burdick and Langston [1977]. However, crustal structure is probably the most important factor contributing to the inconsistency observed in short-period body waves as can be surmised by examining the horizontal components of motion of complicated P-waveforms.

The other operators have been fixed so that we may investigate the operator m(t), the upper mantle response. The earth is assumed to be laterally homogeneous, and the radial velocity structure is approximated by layers of constant velocity. An earth flattening transformation approximates the spherical earth by a plane layered medium. The Green's function is approximated by summing a finite number of generalized rays, the individual ray response is calculated using a Cagniard-de Hoop algorithm [see Helmberger, 1973a for details]. To maximize computations the ray sum is truncated after including all of the primaries for a time period. In ranges where diffraction is important, in shadow zones and off the ends of triplications, multiple reflections were added to test the convergence of ray sum. The accuracy and limitation of this technique is

discussed by Burdick and Orcutt [1979] and will not be reviewed here in the interest of brevity.

At the ranges and for the structures we will be considering, the phase PP is an important consideration. An anomalous later phase can be identified at several stations 12 to 15 sec after the first arrival which we tentatively identified as PP. Preliminary synthetic models of PP indicate that this phase could be large depending on the internal reflections at the surface near the halfway point.

III. DETAILED MODEL DETERMINATION

We will begin this section by presenting our results, namely model K8, followed by a comparison of ($dT/d\Delta$) measurements and travel times with the model predictions. Next, we will give a detailed comparison of the waveform data with synthetics generated from K8.

The starting model KCA and model K8 are shown in Fig. 3 and their corresponding ($dT/d\Delta$) values displayed in Fig. 4. There are two important differences between the models. One is the low velocity zone at 150 km depth in K8. The other is the steep positive velocity gradient between 300 and 400 km in K8 where KCA has a very small gradient.

Travel time curves for the two models are compared in Fig. 5. Plotted with the calculated curves are readings from the ISC for the nuclear explosions in Novaya Zemlya during the period 1966-1974.

However, the inconsistency of observed PP from station to station makes this phase difficult to use as a model discriminant. Upon examination of this figure it should be noted that KCA predicts the travel times at ranges 18 to 22° and 23 to 25° better than K8 although diffracted arrivals tend to prolong the A branch out to at least 18°. Furthermore there appears

to be scattered energy arriving between the Ad and Bd arrivals which can be attributed to high frequency scattering phenomena. It is plausible that diffraction and scattering can extend the Ad branch as far out as 20° making the K8 model more consistent with the data.

The deviation of K8 from the data at around 23° is harder to justify. In this case, we fit the waveform data at the expense of the travel times. It is possible that the discrepancy is indicating that our model is too simple but the data set is not extensive enough to resolve this question.

Crustal structure (0 to 40 km)

The crustal structure of model K8 was taken from KCA which assumed a single 40 km layer with velocity of 6.4 km/sec. This structure was derived from a synthesis of published data by Der and Landisman [1972]. The vertical travel time is consistent with the three layer model derived by Masse and Alexander [1974] and is slightly shorter than the more recently propesed model by Vinnik et al. [1978]. There is undoubtedly some lateral variation off the edges of the east European platform that are larger than the differences between these models and we should expect to see at least a second of scatter in travel times at triplication distances, see Vinnik et al. [1978]. Since the details of the crustal layering has little effect on the synthetic P-waveshapes beyond 9°, we felt justified in choosing the simplest model available.

Lid and Low Velocity Zone (40 to 300 km)

The profiles of long- and short-period observations which were used to interpret the upper 300 km are shown in Fig. 6. The long period data is exclusively from Novaya Zemlya sources, the short-period observations are from Novaya Zemlya and other, smaller explosions to the south. The

closest readable short-period data are at 14.5°. Because of the normal differences in gain settings, we were unable to obtain simultaneous recordings of any one event. However, the multiplicity of both large and small explosions at Novaya Zemlya corroborated our observations of the important features in the data.

The P-waves from 9 to 11.4° are relatively simple pulses suggesting that the propagation path is smoothly varying. The large, later phase at KBS, 11 sec after the first arrival, is most easily explained by PP; however, it is anomalously large at this particular station and it does not appear in most of the other observations.

Beyond 13.3° the waveforms begin to show more complexity, the long- and short-period seismograms showing consistent features which are interpreted as upper mantle structure. The most obvious feature on these records is the onset of the CD branch, the reflection from the 400 km discontinuity. Beyond 15° this phase dominates both the long- and short-period seismograms. Another consistent observation is the small long-period first arrival at 14.5° which grows weaker with distance, becoming almost unobservable on the seismogram in Fig. 6. A second phase becomes apparent on the long-period data at UME 2-3 sec after the first arrival. This second phase is also consistently verified on the short-period seismograms although it is of a variable nature. The onset of the second arrival, and the dramatic decay of the amplitude of the first arrival is crucial to the argument for the existence of a low velocity zone near 200 km.

We perturbed the initial model KCA, to fit the long-period records at UME and NUR beyond 15° while trying to preserve the simple nature of the waveforms at the nearer ranges. Our best effort at matching the long-

period features is displayed in Fig. 7 where we have included the synthetics for model KCA for comparison. As mentioned earlier the convolution of the source function given in the right-hand corner with the derivative of the step responses yield the synthetics. Note that by including the LVZ we were able to produce the double arrival with the proper decay of the initial arrival, P(Ad) with range.

The corresponding short-period synthetics are displayed in Fig. 8. The relative timing of the phases in the synthetics are consistent with the data as well as some of the relative amplitudes.

Transition Region (300 to 800 km)

The seismograms used in modeling the transition region are particularly interesting as can be surmised by noting the intersections of the triplication plots in Fig. 5.

As in the previous section, we relied heavily on the long-period waveform data in determining the branch positions and the resulting model. The synthetics and representative waveforms for these ranges are displayed in Fig. 9. The observed waveforms are somewhat variable in quality. For instance, the KON (21.1°) observation is the only seismogram at that range from an explosion at the southern Novaya Zemlya site and is a weak recording. On the other hand, KON (21.9°) is from the northern site where large shots were abundant, some examples are given in Fig. 10 where events 1 and 2 are the same events pictured in Fig. 7. Thus, we considered this waveform as particularly worthwhile to model. The same situation occurs for the COP (24.6°) observation. In general, these waveforms are extremely difficult to model using a trial and error inversion technique because each record is essentially an interference phenomenon where

small changes in the source, see Fig. 10, or model, see step responses, can drastically alter the waveform.

One of the principle differences between K8 and KCA is the gradient above the 400 km discontinuity. Part of the difference is due to the low velocity zone which changes the bottoming depth of rays from above 420 km. To predict correctly the relative arrival times we increased the gradients between 300 and 4-0 km and reduced the size of the 400 km discontinuity. With these changes we were able to model the interference at 21.9° and the cut-off of the long-period AB branch. At 21.1° the relative arrival times of the phases predicted by K8 fit better than those calculated for KCA. However there is some mismatch in the relative amplitudes with the arrival from above the 420 km discontinuity being too large. The choice of velocity gradient below 270 km depends crucially on how we modeled the low velocity zone. Any errors in determining the model or any lateral heterogeneity in the upper 250 km will seriously affect our inversion for the structure between 280 and 400 km. The uncertainties in K8 are probably greatest in this depth range.

The evidence for a discontinuity at 675 km is clear in King and Calcagnile's array data and in our long- and short-period observations. The reflection is first evident at KON, 21.1°, and forms a clear distinct pulse at 23.3° (COP) where the E-F phase is the second pulse. At 25.1° AKU, the E-F arrival is first and the shoulder on the waveform is interpreted to be the C-D phase moving back. The best data showing the position of D on the E-D branch is displayed in Fig. 11 where the observations obtained from the Semipalatinsk test site are compard with synthetics. Due to fortuitous instrument setting near 26° we were able to obtain short- and long-period responses for the same explosions. The waveforms appear to be

of excellent quality and are reproducible for many events. A careful examination of the short-period responses at this particular station indicates that it is relatively transparent as judged from azimuthal and horizontal motion tests [see Helmberger and Wiggins, 1971 for a more detailed description]. For this reason, we have spent much effort in modeling these short- and long-period observations as closely as possible. The main consequence of these efforts is the increased velocity gradient between 670 and 750 km, see Fig. 2, which increases the amplitude of the first arrival. Such a feature is also consistent with the long-period observations at AKU (25.1°). At still larger ranges, we see no compelling evidence of either the (ED) or (AB) branch although the short-period observations are somewhat perplexing with respect to the latter branch, see Figs. 12 and 13.

If we restrict our attention to only NZ events we see relatively simple seismograms beyond 27° which are in agreement with our model. On the other hand, Kazakh events tend to show a major secondary arrival out to larger ranges (labeled by an arrow in Figs. 12 and 13). Since King and Calcagnite [1976] used mostly Kazakh events we can see why their AB branch extends to larger ranges. This feature in the synthetics for their model is the result of the low gradient above 420 km. Thus, this difference in data suggests lateral variations in velocity as deep as 400 km with respect to northern and southern Eurasia. The difficulties with this interpretation are that events from Semipalatinsk do not show this feature, see Fig. 11, and that many Kazakh events do not show this branch, for example see KEV (10) and STU (16). It should also be noted that the onset of the AB branch becomes less impulsive with distance and looks more like the onset of

the AB branch becomes less impulsive with distance and looks more like the onset of a wavetrain, see Figs. 2k-2m of King and Calcagnite [1976]. Perhaps, this phenomenon could be caused by multipathing due to small scale irregularities. It would be particularly interesting to obtain some long-period seismograms that sample this region so that a comparison similar to Fig. 14 could be made.

IV. DISCUSSION

It is interesting to compare model K8 with models proposed for western United States (WUS), see Fig. 15, where the same basic modeling techniques were applied. Models HWA and HWB were derived from the $(dT/d\Delta)$ measurements [Johnson, 1967], the travel times from the NTS explosions and short-period waveform data as discussed earlier. The travel times and (δt) separations between the triplication arrivals for HWB and HWA are substantially different between 13 and 19°, where the first arrivals appropriate for the HWA region is from 3 to 6 sec later than for HWB. Model T7 was constructed to fit the HWA data set as well as the long-period waveforms obtained from a series of well-studied earthquakes. On the other hand, the travel times and (δt)'s for the model HWB are compatible with those predicted by K8. Furthermore, a comparison of the short-period seismograms displayed in Fig. 6 are quite similar to the short-period profile presented by Helmberger and Wiggins [1971], Fig. 2. At ranges beyond 20°, the distinction between the regionalization HWA and HWB disappears and there appears to be little evidence of lateral velocity variations below 300 km. Note that T7 and K8 are remarkably similar in structure below this depth. The slight off-sets in discontinuities reflect the lid and LVZ disparity which is worth a brief review.

The upper 200 km of T7 was constructed to fit the average travel times and amplitude properties of WUS where there appears to be an effective shadow zone along some profiles, see Helmberger [1973b]. This effect can be caused by a LVZ as in T7 but it could be caused by lateral changes in velocity when crossing the various structural provinces, for instance see York and Helmberger [1973]. Thus, the basic vertical structure of HWA or K8 may be appropriate for some portions of northern WUS and the known short-period amplitude pattern caused by horizon change in structure. Small changes in the velocity structure of the Lid and LVZ can make a dramatic change in synthetic seismograms at the near-in distances of 8 to 19° as can be seen by the following case study.

In collecting a data set of seismograms one invariably finds an odd observation which appears incompatible in travel time and wave-shape with the others, such is the case with the NUR record displayed in Fig. 16. NUR is a recording of a southern Novaya Zemlya event whereas UME was produced by a northern Novaya Zemlya event, see Fig. 1. As with nearly all of the long-period observations, the NUR record is duplicated for two different events so that an unusual source function does not appear to be a likely explanation for the difference in waveforms. Explaining this record in terms of a perturbation of model K8 proved to be quite easy and enlightening. By slowing the first arrival by about 1 sec relative to the reflection from below the low velocity zone and the 420 km discontinuity, we can reproduce the relative timing of the seismograms. The result is model K8' shown in Fig. 16. Note that we have also slightly decreased the depth to the low velocity zone. Another characteristic of the model is that a critically reflected

arrival now comes from below the low velocity zone; i.e., the shadow zone ends at 15° rather than 19°. This feature substantially increases the amplitude of the second arrival relative to the C-D reflection.

We conclude that the upper mantle in northwestern Eurasia is somewhat variable. Model K8 may average over variations as large as those between K8 and K8' so that the detailed features of K8 may be considered to be exemplary. The trade-offs involved in modeling low velocity zones are well known, see Dowling and Nuttli [1964], Helmberger [1973b]. To more fully constrain the features of a low velocity zone we need to incorporate longer period data from earthquake sources. Fig. 18 complements Figs. 16 and 17 by comparing long-period and short-period synthetics for K8 and K8'. The long-period seismograms are from an earthquake source appropriate for the March 23, 1978 Bermuda event (Gordon Stewart, work in progress). The long-period seismograms are very similar, hence their usefulness in constraining the overall features of the model such as the average gradients and the sizes of discontinuities. The short-period data are more sensitive to small scale details. The need to consider broad-band information, long- and short-period waveshapes as well as $dT/d\Delta$ and travel time data, is obvious from this series of figures.

The major new feature in model K8 is the low velocity zone and it is based on the long- and short-period observations between 9 and 18°. It is not possible to completely rule out a simple discontinuity at 220 km depth as has been suggested by Lehmann [1964, 1967] for the U.S. Several models including such a feature were tested but none were found that fit the data as well as K8. Such a model would be required to have a nearly constant velocity over substantial region of the upper 400

km. In addition, a different Q structure than implied in this study would be necessary to predict the correct amplitude behavior of the travel time branches. As our knowledge of the velocity and Q structure of the earth increases the data is, of course, subject to reinterpretation under other working hypotheses.

It is unfortunate that we do not have a very dense coverage of long-period receivers at distances of 19-25°. The high frequency explosion source would have been ideal for elucidating any additional structure between the two major discontinuities. Models HWB, SMAK [Simpson et al., 1976], and ARC-TR [Fukao, 1977] all have an inflection in the velocity structure at about 550 km. Burdick and Helmberger [1978] have pointed out the difficulties in observing this feature: the short-period data have too much resolving power, the long-period earthquake data have too little. We found no direct evidence to justify including such a feature; however, considering the discrepancies in the observed and predicted waveforms, the structure between the two discontinutieis remains somewhat uncertain.

In summary, we have incorporated the long-period and short-period waveforms data with travel time and apparent velocity measurements to derive the model K8 (Table 2) for Northwest Eurasia. The significant features of the model are:

(1) A low velocity zone between depths of 150 and 200 km;

(2) A 4.5% velocity increase at 420 km depth;

(3) A large velocity gradient between 420 and 675 km;

(4) A 4% velocity increase at 675 km depth.

Model K8 is similar to model T7 proposed recently for the Western United States; however, without a detailed determination of the uppermost velocity structure, any discussion of lateral heterogeneity is premature.

ACKNOWLEDGEMENTS

We wish to thank G. Engen, L. Burdick and D. Anderson for critically reading the manuscript. This research was supported by the Advanced Research Projects Agency of the Department of Defense and was monitored by the Air Force Office of Scientific Research under Contract F44620-72-C-0083. Contribution No. 3311, Division of Geological and Planetary Sciences, California Institute of Technology, Pasadena, California 91125.

References

Burdick, L. J., and D. V. Helmberger, The upper mantle P-velocity structure of the western United States, J. Geophys. Res., 83, 1699-1712, 1978.

Burdick, L. J., and D. V. Helmberger, Time functions appropriate for nuclear explosions, Bull. Seismol. Soc. Am., 69, 951, 1979.

Burdick, L. J. and C. A. Langston, Modeling crustal sturcture through the use of converted phases in teleseismic body waveforms, Bull. Seism. Soc. Am., 67, 677-691, 1977.

Burdick, L. J., and J. A. Orcutt, A comparison of the generalized ray and reflectivity methods of waveform synthesis, Geophys. J. R. ast. Soc. (in press).

Carpenter, E. W., Absorption of elastic waves - an operator for a constant Q mechanism. AWRE Report No. 0-43/66, 16 pp, 1966.

Der, Z. A., and M. Landisman, Theory of errors, resolution and separation of unknown variables in inverse problems with application to the mantle and the crust in southern Africa and Scandanavia, Geophys. J. R. astr. Soc., 27, 137, 1972.

Dowling, J., and O. Nuttli, Travel time curves for a low velocity channel in the upper mantle, Bull. Seism. Soc. Am., 54, 1981, 1964.

Dey-Sarkar, S. K., and R. A. Wiggins, Upper mantle structure in Western Canada, J. Geophys. Res., 81, 3619, 1976.

Fukao, Y., Upper mantle p-structure at the trench side of the Japan-Kurite arc, Geophys. J. R. astr. Soc., 50, 621, 1977.

Futterman, W. I., Dispersive body waves, J. Geophys. Res., 67, 5279, 1962.

Helmberger, D. V., Numerical seismograms of long period body waves from seventeen to forty degrees, Bull. Seism. Soc. Am., 64, 45, 1973a.

Helmberger, D. V., On the structure of the low velocity zone, Geophys. J. R. Astr. Soc., 34, 241, 1973b.

Helmberger, D. V., and L. J. Burdick, Synthetic seismograms, Ann. Rev. Earth Planet. Sci., 7, 417, 1979.

Helmberger, D. V., and R. A. Wiggins, Upper mantle structure of the midwestern United States, J. Geophys. Res., 76, 3229, 1971

Johnson, L. R., Array measurements of P-velocities in the upper mantle, J. Geophys. Res. 92, 6309, 1967.

Kennett, B.L.N., The effects of attenuation on seismograms, Bull. Seism. Soc. Am., 65, 1643, 1975.

King, D. W., and G. Calcagnite, P-wave velocities in the upper mantle beneath Fennoscandia and Western Russia, Geophys. J. R. Astr. Soc., 46, 407, 1976.

Lehmann, I., On the travel times of P as obtained from the nuclear explosions Bilby and Shoal, Phys. Earth and Planet. Int., 1, 14-23, 1967.

Lehmann, I., The travel times of the longitudinal waves of the Logan and Blanca atomic explosions and their velocities in the upper mantle, Bull. Seism. Soc. Am., 52, 519, 1962.

Masse, R. P., and S. S. Alexander, Compressional velocity distribution beneath Scandanavia and Western Russia, Geophys. J. R. Astr. Soc., 39, 587, 1974.

Romney, C., B. G. Brooks, P. H. Mansfield, D. S. Carder, J. N. Jordan, and D. W. Gordon, Travel times and amplitudes of principal body phases recorded from Gnome, Bull. Seism. Soc. Am., 57, 829, 1962.

Simpson, D. W., R. F. Mereu, and D. W. King, Array study of P-wave velocities in the upper mantle transition zone beneath Northeastern Australia, Bull. Seism. Soc. Am., 61, 1751, 1974.

Vinnik, L. P., V. Z. Ryaboy, L. N. Starobinets, A. V. Egorkin, and N. M. Chernyshev, Velocities of P-waves in the upper mantle of the East European platform, Proc. (Dokl.) Acad. Sci. USSR, 244, 70, 1978 (in Russian).

York, J. E., and D. V. Helmberger, Low velocity zone variations in the southwestern United States, J. Geophys. Res., 78, 1883, 1973.

Wiggins, R. A., Monte Carlo inversion of body wave observations, J. Geophys. Res., 74, 3171, 1969.

Wiggins, R. A., and D. V. Helmberger, Upper mantle structure of the western United States, J. Geophys. Res., 78, 1870, 1973.

von Seggern, D., and R. Blanford, Source time functions and spectra for underground nuclear explosions, Geophys. J. R. Astr. Soc., 31, 83, 1972.

Table 2. Velocity Model K8. Depths Are to Top of Layer

Velocity	Depth	Velocity	Depth	Velocity	Depth	Velocity	Depth
6.39	0	8.392	250	9.572	496	10.955	749
6.40	1	8.419	260	9.583	506	10.998	759
8.170	40	8.445	270	9.624	517	11.040	770
8.187	50	8.478	280	9.667	528	11.061	783
8.205	60	8.511	290	9.708	539	11.083	796
8.222	70	8.545	300	9.750	550	11.105	808
8.239	80	8.578	310	9.792	560	11.127	821
8.256	90	8.612	320	9.834	570	11.148	834
8.274	100	8.645	330	9.876	580	11.170	847
8.291	110	8.678	340	9.818	590	11.192	859
8.308	120	8.712	350	9.960	604	11.213	872
8.325	130	8.745	360	10.003	610	11.235	885
8.343	140	8.764	370	10.045	620	11.256	898
8.250	150	8.783	380	10.090	631	11.278	911
8.180	155	8.803	391	10.135	641	11.300	923
8.050	160	8.822	400	10.180	653	11.321	936
8.040	170	8.841	410	10.225	664	11.343	949
8.150	180	9.24	420	10.660	675	11.365	962
8.270	190	9.292	431	10.702	686	11.385	974
8.287	200	9.333	442	10.744	696	11.408	987
8.305	210	9.375	452	10.789	707		
8.323	220	9.415	467	10.829	717		
8.340	230	9.458	474	10.891	728		
8.366	240	9.50	485	10.913	738		

Table 1. Nuclear Explosions

Event No.	Date	Hr:Min:Sec	Lat E	Lon N	
1	08/28/72	5:59.57	73.30	55.1	Novaya Zemlya N
2	09/27/71	5:59.55	73.40	55.1	Novaya Zemlya N
3	11/02/74	4:59.57	70.80	53.91	Novaya Zemlya S
4	10/27/73	6:59.57	70.80	54.20	Novaya Zemlya S
5	09/12/73	6:59.54	73.30	55.20	Novaya Zemlya N
6	10/27/66	5:58.00	73.38	54.62	Novaya Zemlya S
7	07/10/71	17:00.00	64.2	54.77	
8	11/08/68	10:02.05	73.40	54.90	Novaya Zemlya N
9	08/14/74	14:59.58	68.91	75.90	
10	09/26/69	6:59.56	45.89	42.47	Kazakh E
11	08/20/72	2:59.58	49.46	48.18	Kazakh N
12	10/22/71	6:02.57	51.51	54.54	
13	09/27/73	6:59.58	70.76	53.87	Novaya Zemlya S
14	07/01/68	4:02.02	47.92	47.95	Kazakh N
15	10/03/72	8:59.58	46.85	45.01	Kazakh E
16	12/22/71	6:39.56	47.87	48.22	Kazakh N
17	12/06/69	7:02.59	43.83	54.78	Kazakh W
18	12/12/71	7:00.57	43.85	54.77	Kazakh W
19	12/23/70	7:00.57	43.83	54.85	Kazakh W
20	02/13/66	4:51.58	49.82	78.13	Semipalatinsk
21	07/23/73	1:22.58	49.99	78.85	Semipalatinsk
22	12/18/66	4:57.58	49.93	77.73	Semipalatinsk
23	02/26/67	3:57.58	49.78	78.12	Semipalatinsk

Figure Captions

Figure 1. Map indicating the locations of source events and WWSSN seismographs used in this study. Information about the event numbers is given in Table 1.

Figure 2. Long-period, vertical component seismogram, KEV from Novaya Zemlya (8/28/72) recorded at $\Delta = 9.4°$. The s-phase is much larger than the p-phase and has virtually the same frequency content.

Figure 3. Model KCA and K8.

Figure 4. Comparison of the $(dT/d\Delta)$ measurements reported by King and Calcagnite [1976] and K8 predictions.

Figure 5. Comparison of predicted travel time curve for K8 and KCA and travel times of Novaya Zemlya explosions as reported by the ISC. The letters on the K8 travel time plot label the branches for further reference in the text. Solid lines indicate direct ray theoretical arrivals, dashed lines indicate the prolongation of certain branches by diffraction due to a low velocity zone.

Figure 6. Representative seismograms obtained from Novaya Zemlya explosions displaying various arrivals. The lines are keyed to the triplication plots given in Fig. 4. The number following the station label indicates the event (Table 1) where 1 and 2 are from the northern site.

Figure 7. Comparison of synthetics with the long-period waveform data.

Figure 8. Short-period synthetics for KCA and K8 which can be compared with the data in Fig. 6.

Figure 9. Comparison of the observed waveforms with synthetics. The K8 synthetics were produced by a convolution of the source function displayed in the right-hand corner with the derivative of the step responses.

Figure 10. Comparison of synthetic (K8) with observations from various events at the Northern Novaya Zemlya test site indicating source variability.

Figure 11. Observations at Tabriz, Iran from nuclear explsions in Semipalatinsk. The data clearly show evidence for the 675 km discontinuity and the position of the end of the C-D branch.

Figure 12. Theoretical seismograms from K8 fit the short-period seismograms as well as KCA. The inconsistency of the records between 24 and 25° should be noted. The large later phase indicated by the arrows is similar to the arrival of King and Calcagnite [1976] interpreted as the reflection from the 420 km discontinuity.

Figure 13. The figure compares theoretical and observed seismograms from 25 to 29°. Again note the occasional appearance of the reflection from the 420 km discontinuity. This appears to be a regional phenomena, observed only on sources in Kazakh and receivers in Northwest Europe.

Figure 14. The figure shows the theoretical and observed seismograms of Novaya Zemlya explosions recorded at STU. Model KCA still predicts a large reflection from the 420 km discontinuity which is not evident in the data.

Figure 15. Comparison of model K8 with models HWA, HWB, and T7 derived from WUS observations.

Figure 16. Seismograms from Northern Novaya Zemlya to UME and from Southern Novaya Zemlya to NUR. These seismograms are along slightly different azimuths. The difference can be explained by variation in the velocity structure above 180 km (see Fig. 17).

Figure 17. Model K8' which was derived from K8 to explain the variation at 15.6°, see Fig. 16.

Figure 18. Short- and long-period synthetics for K8 and K8'. The long-period source function is from the March 23, 1978 Bermuda earthquake (G. Stewart, personal communication).

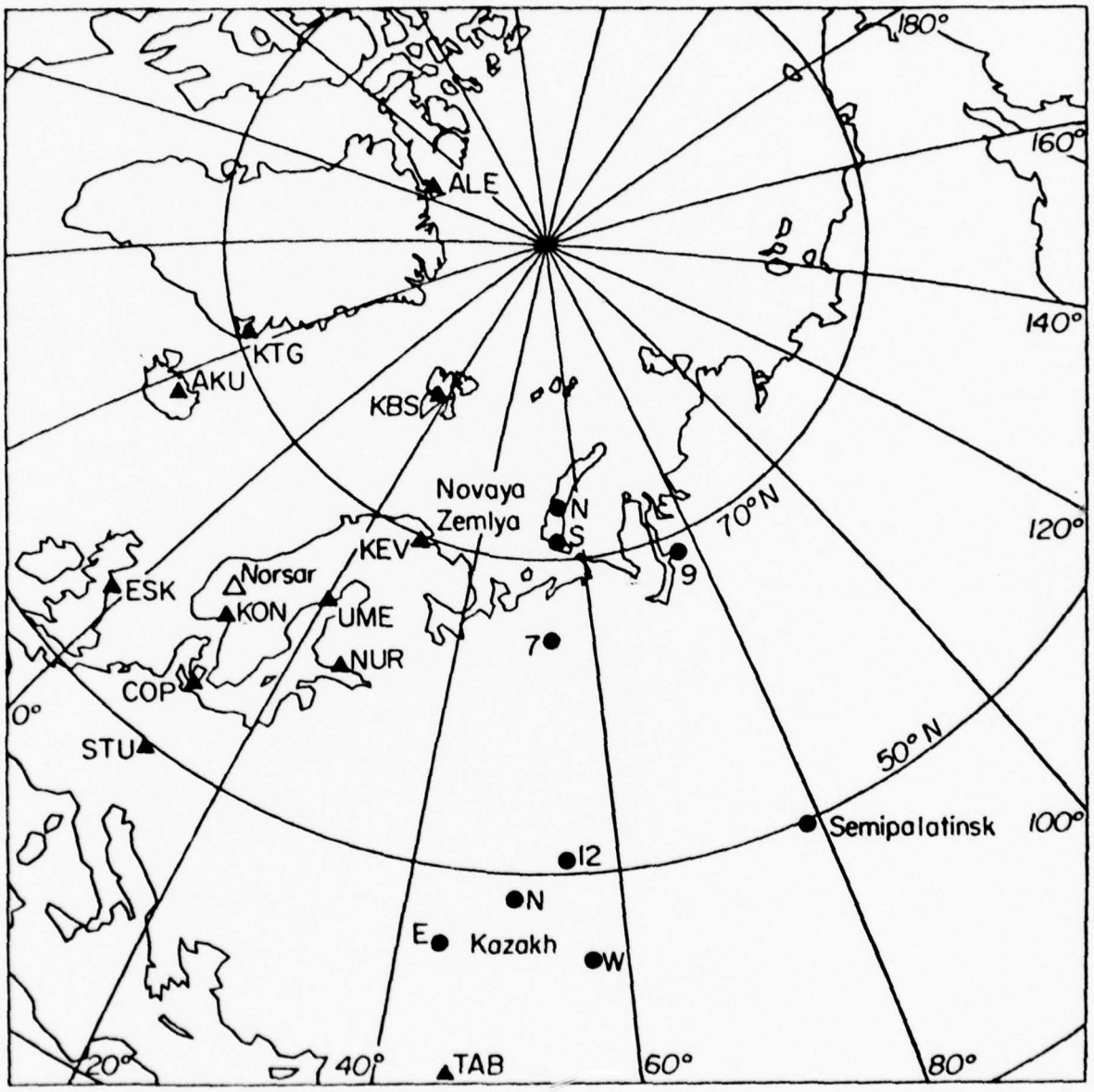
180°
160°
140°
120°
70°N
50°N
100°
80°
60°
40°
20°
0°
ALE
KTG
AKU
KBS
Novaya
Zemlya
N
S
KEV
ESK
Norsar
KON
UME
NUR
COP
STU
9
7
12
N
E
Kazakh
W
Semipalatinsk
TAB

Fig. 1

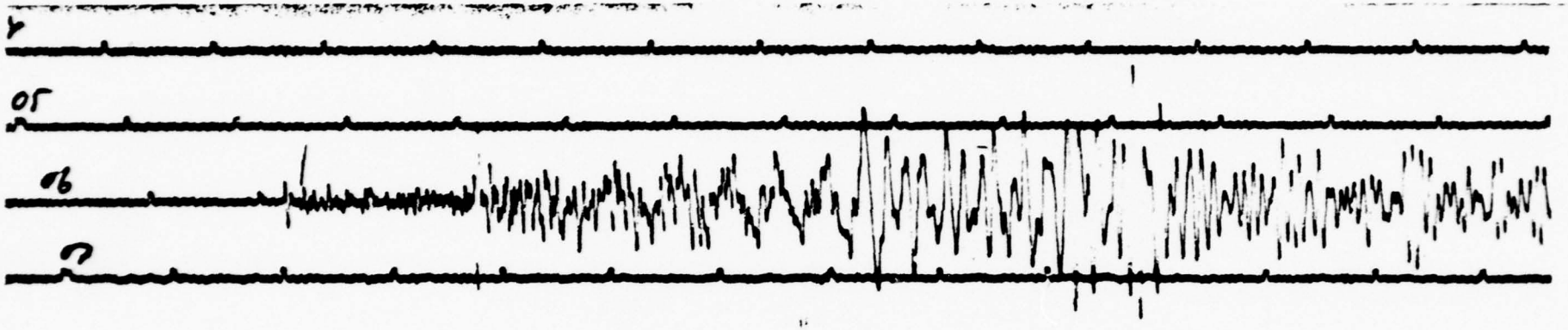

Fig. 2

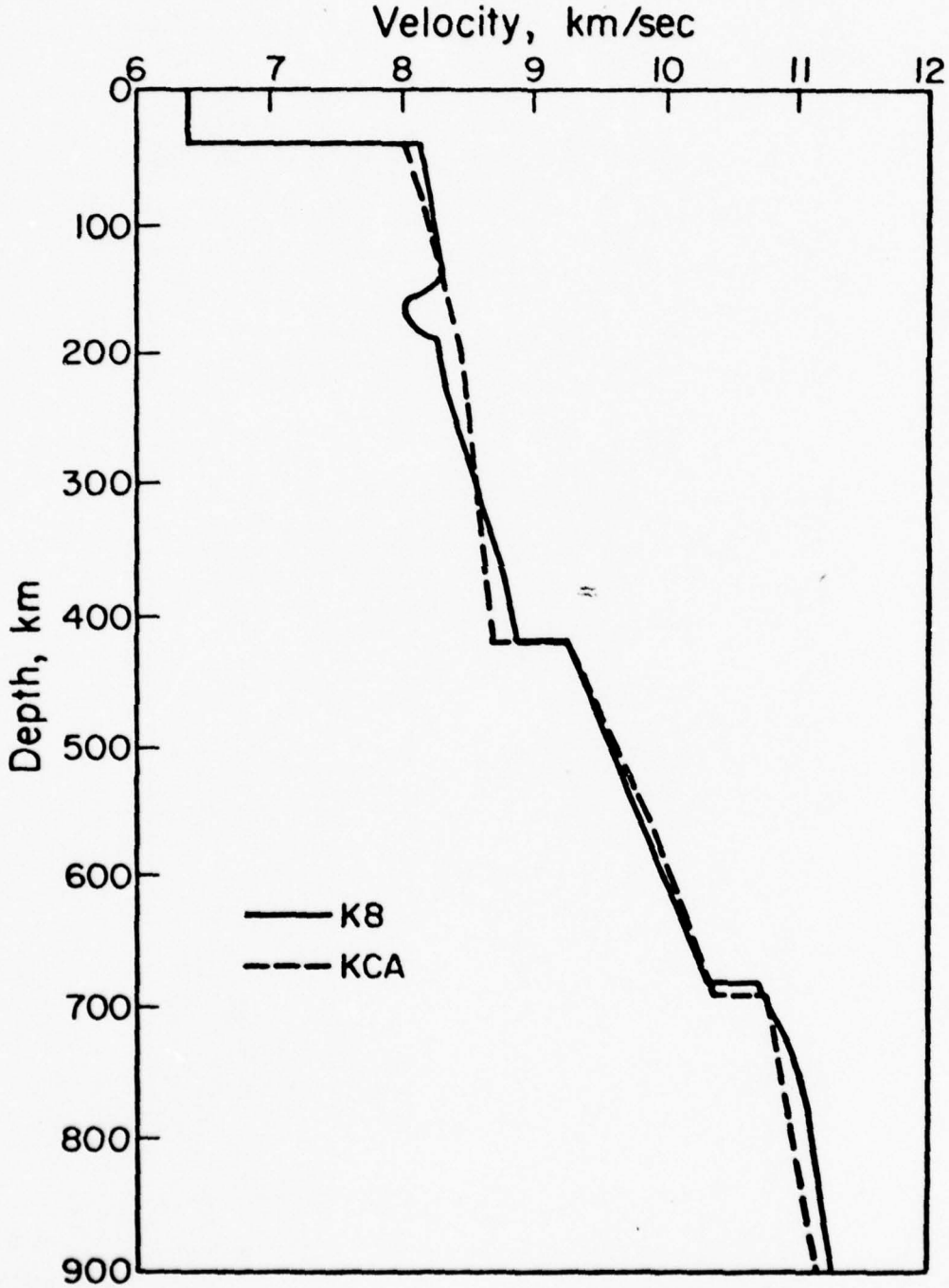
Velocity, km/sec
6
7
8
9
10
11
12
0
100
200
300
400
500
600
700
800
900
Depth, km
K8
KCA

Fig. 3

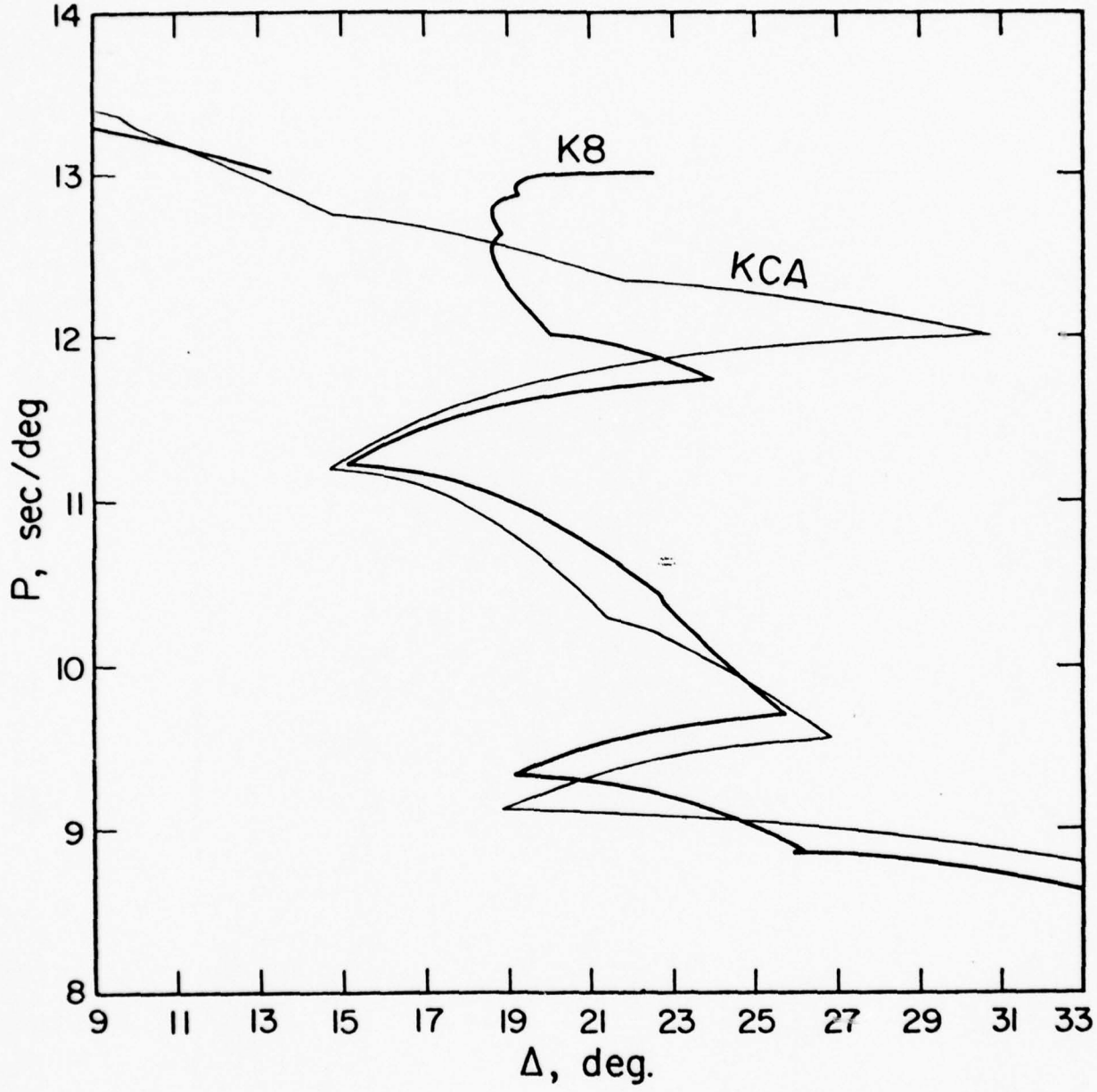
K8
KCA
P, sec/deg
Δ, deg.
14
13
12
11
10
9
8
9
11
13
15
17
19
21
23
25
27
29
31
33

Fig. 4

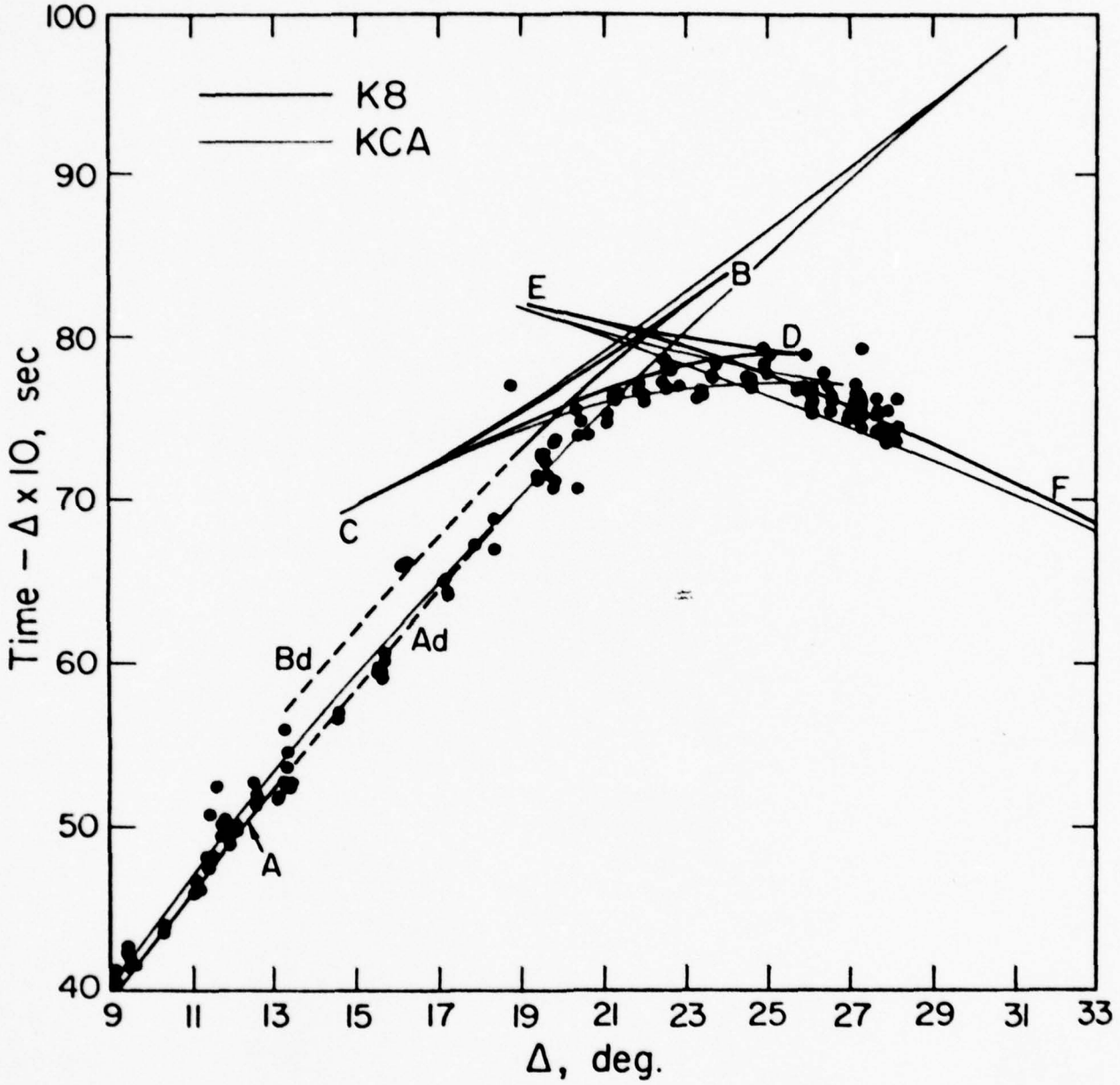
K8
KCA
A
B
C
D
E
F
Ad
Bd
Time − Δ x 10, sec
Δ, deg.
100
90
80
70
60
50
40
9
11
13
15
17
19
21
23
25
27
29
31
33

Fig. 5

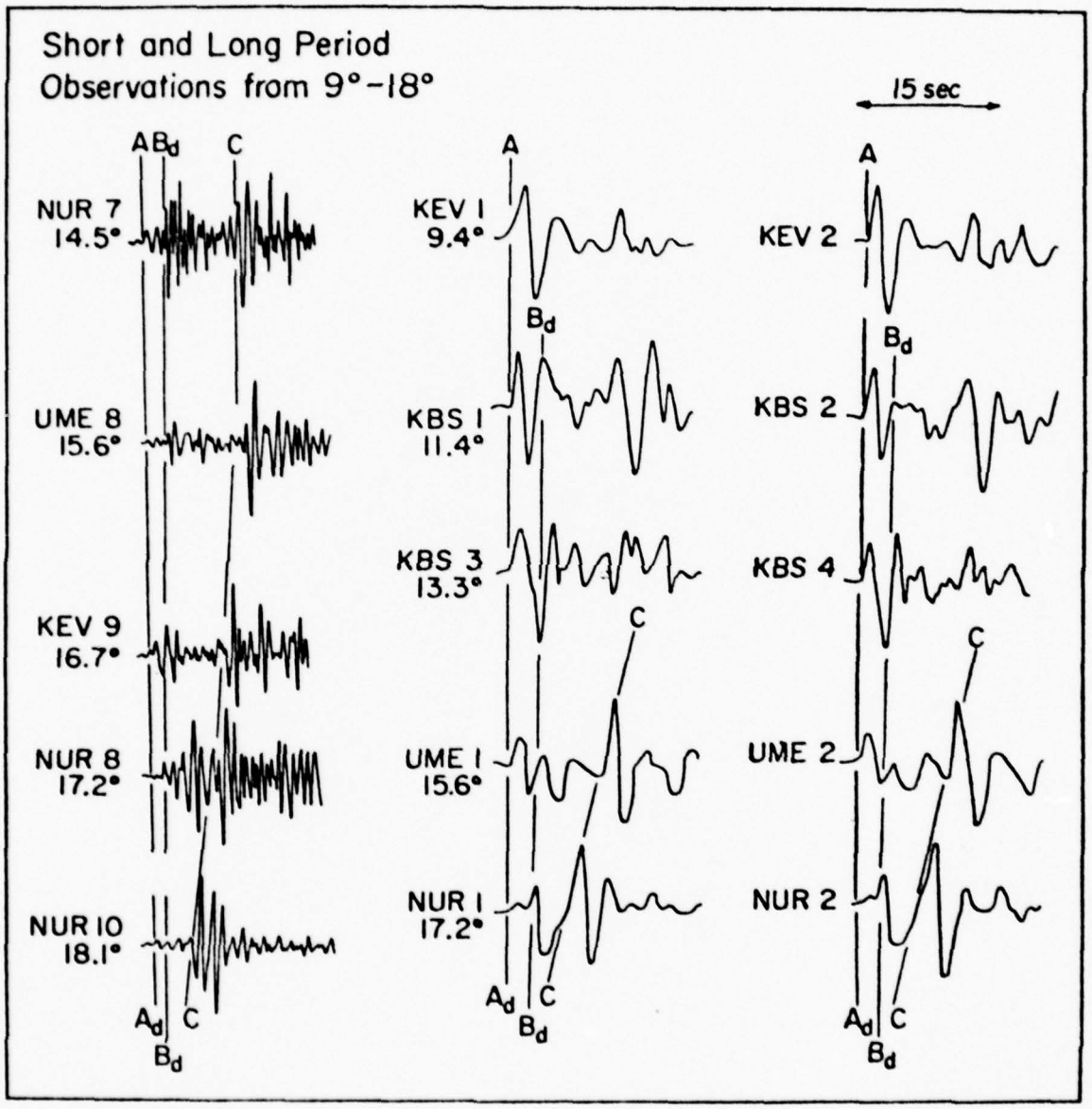
Short and Long Period
Observations from 9°-18°
15 sec
NUR 7
14.5°
UME 8
15.6°
KEV 9
16.7°
NUR 8
17.2°
NUR 10
18.1°
KEV 1
9.4°
KBS 1
11.4°
KBS 3
13.3°
UME 1
15.6°
NUR 1
17.2°
KEV 2
KBS 2
KBS 4
UME 2
NUR 2
A
Bd
C
Ad

Fig. 6

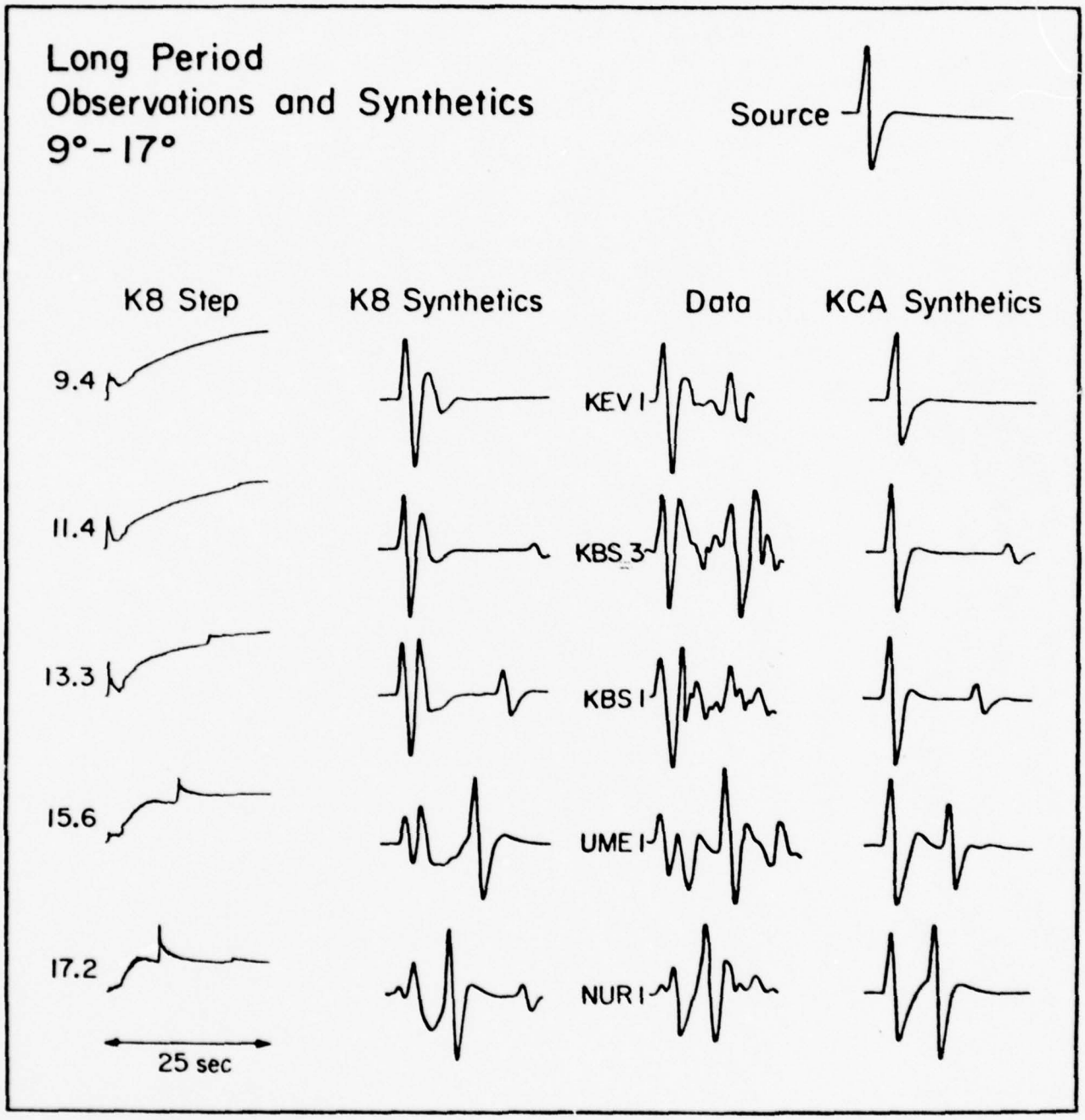
Long Period
Observations and Synthetics
9°-17°
Source
K8 Step
K8 Synthetics
Data
KCA Synthetics
9.4
11.4
13.3
15.6
17.2
KEV I
KBS 3
KBS I
UME I
NUR I
25 sec

Fig. 7

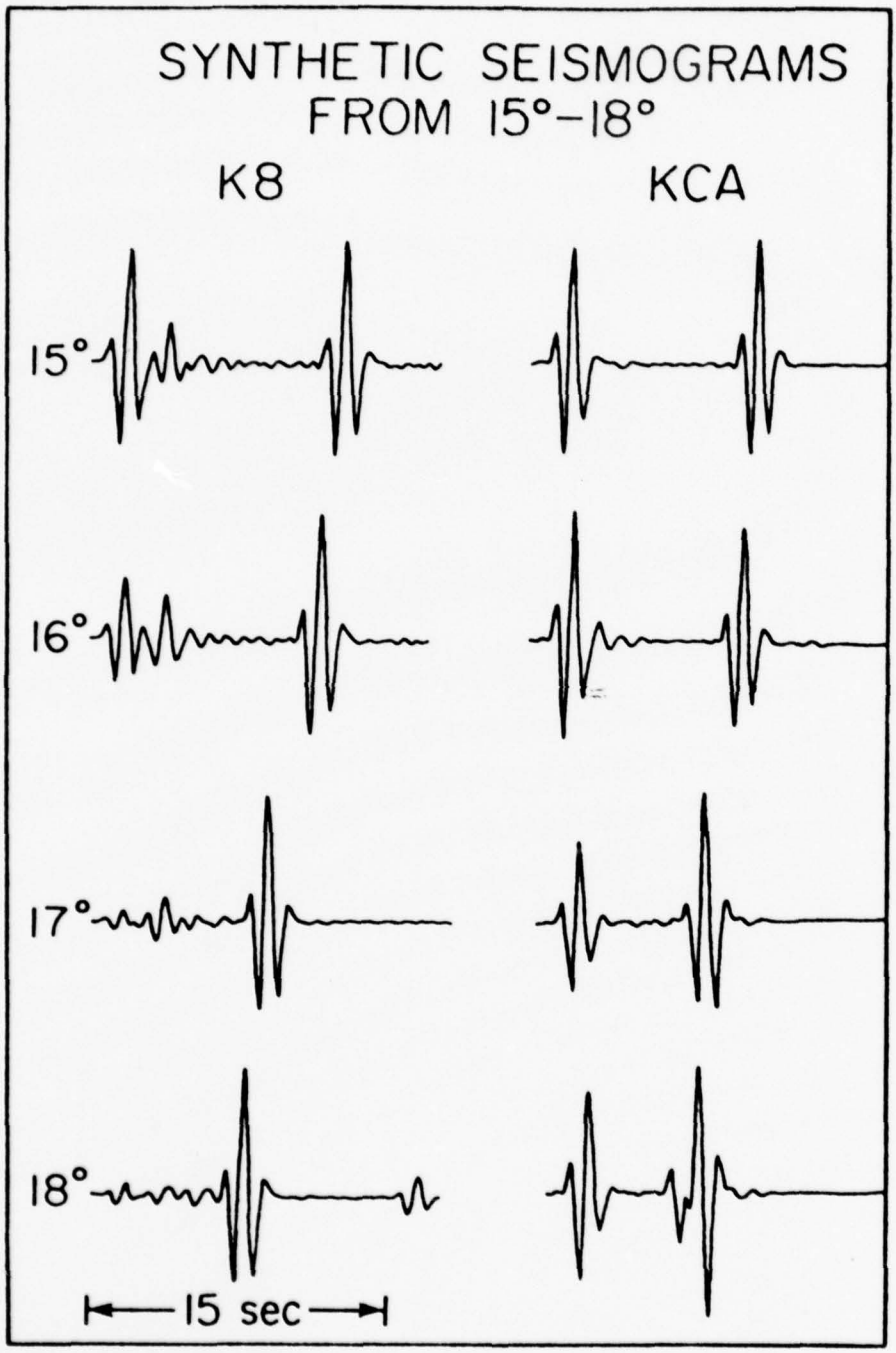

Fig. 8

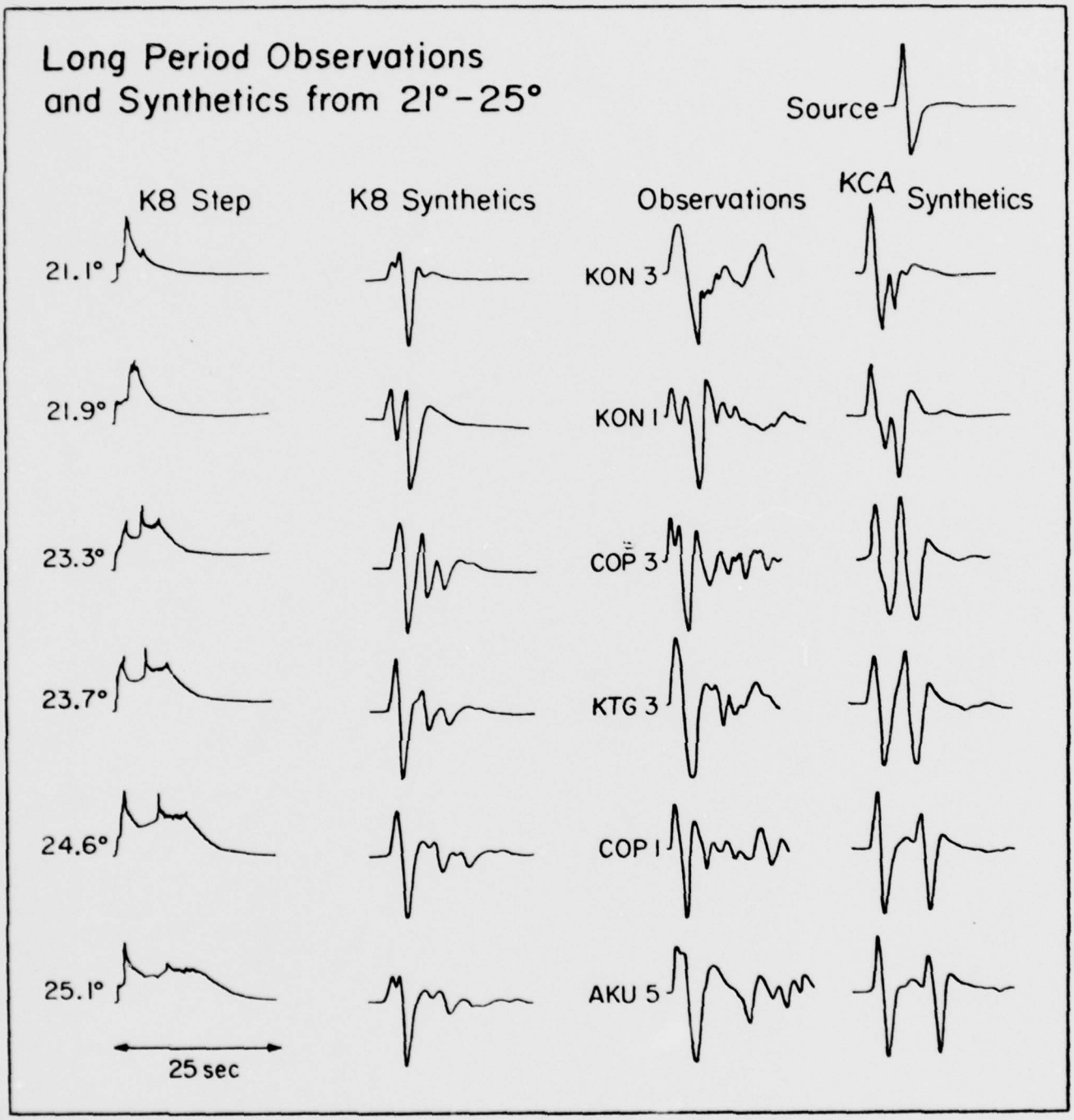
Long Period Observations
and Synthetics from 21°-25°
Source
K8 Step
K8 Synthetics
Observations
KCA
Synthetics
21.1°
21.9°
23.3°
23.7°
24.6°
25.1°
KON 3
KON 1
COP 3
KTG 3
COP 1
AKU 5
25 sec

Fig. 9

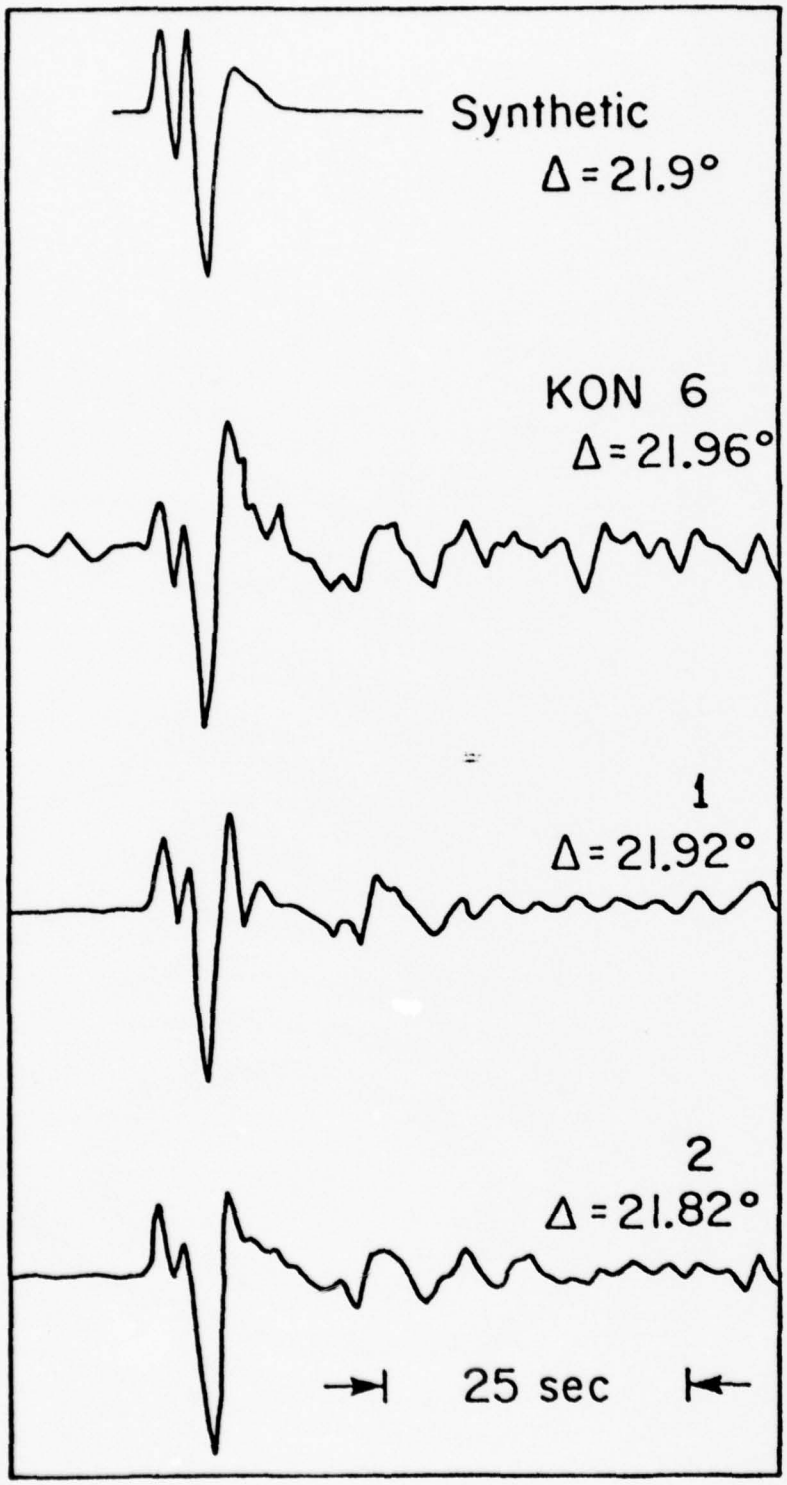

Fig. 10

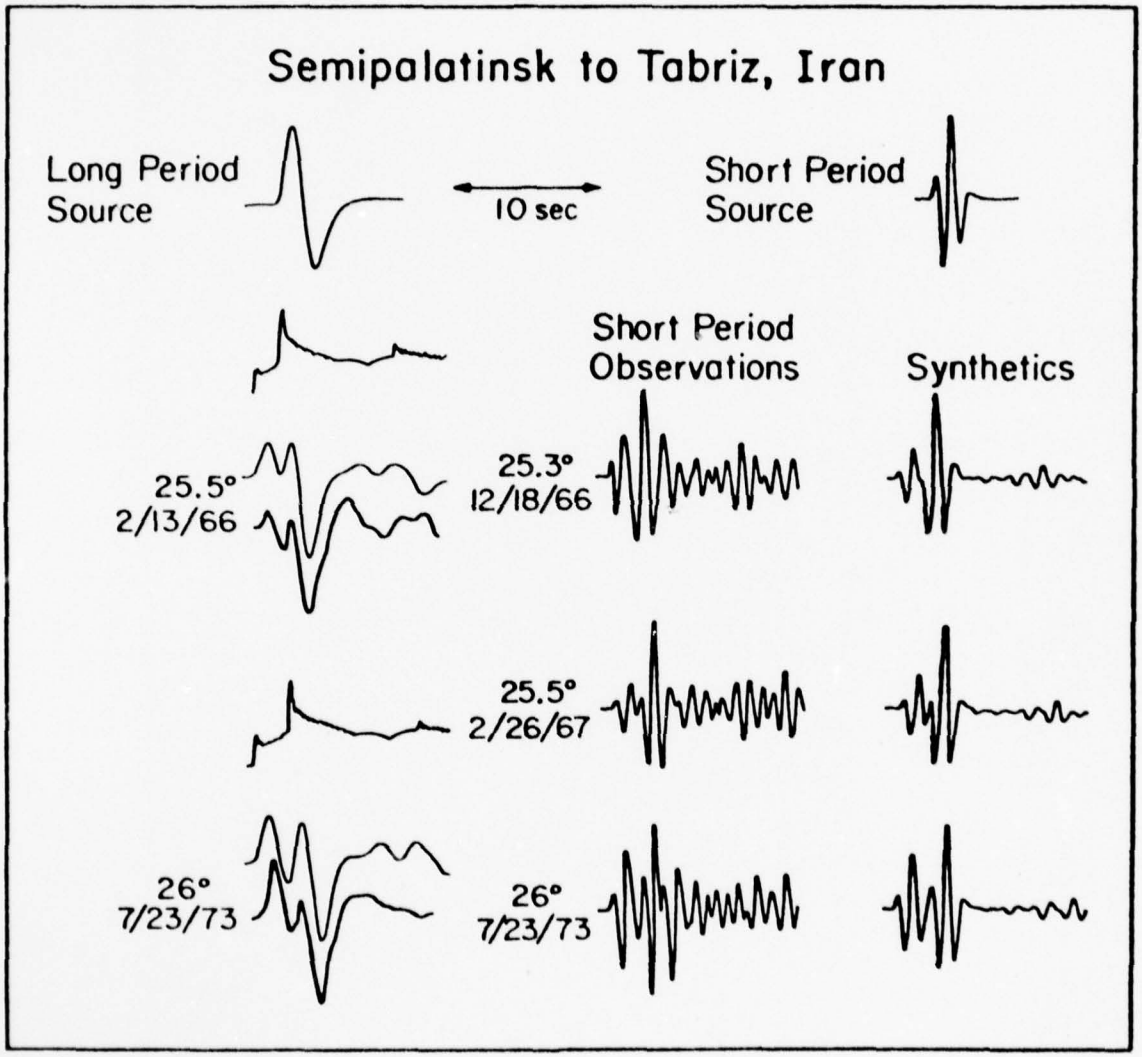
Semipalatinsk to Tabriz, Iran
Long Period Source
10 sec
Short Period Source
Short Period Observations
Synthetics
25.5°
2/13/66
25.3°
12/18/66
25.5°
2/26/67
26°
7/23/73
26°
7/23/73

Fig. 11

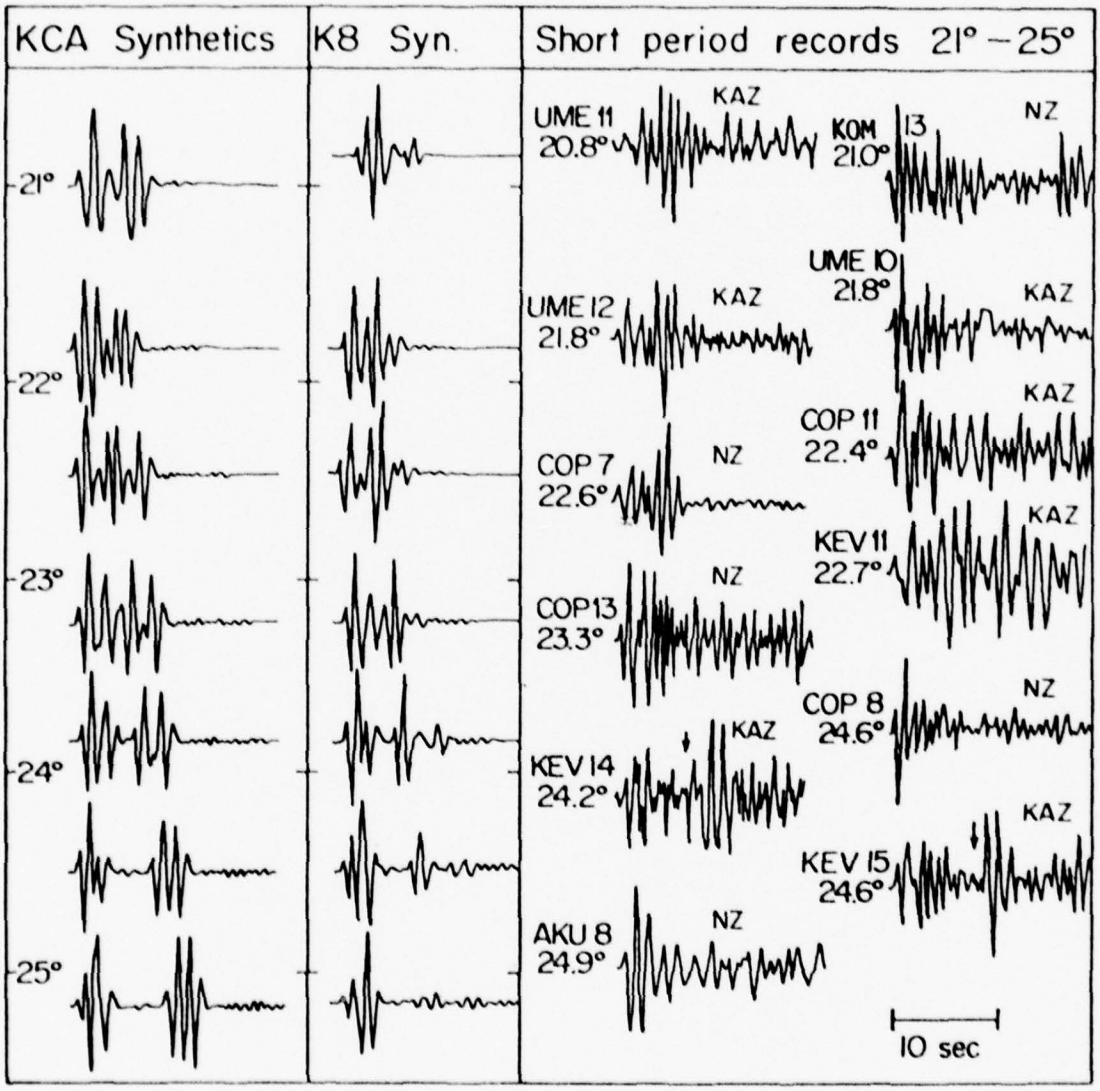
KCA Synthetics
K8 Syn.
Short period records 21° – 25°
21°
22°
23°
24°
25°
UME 11
20.8°
KAZ
KOM 13
21.0°
NZ
UME 10
21.8°
KAZ
UME 12
21.8°
KAZ
COP 11
22.4°
KAZ
COP 7
22.6°
NZ
KEV 11
22.7°
KAZ
COP 13
23.3°
NZ
COP 8
24.6°
NZ
KEV 14
24.2°
KAZ
KEV 15
24.6°
KAZ
AKU 8
24.9°
NZ
10 sec

Fig. 12

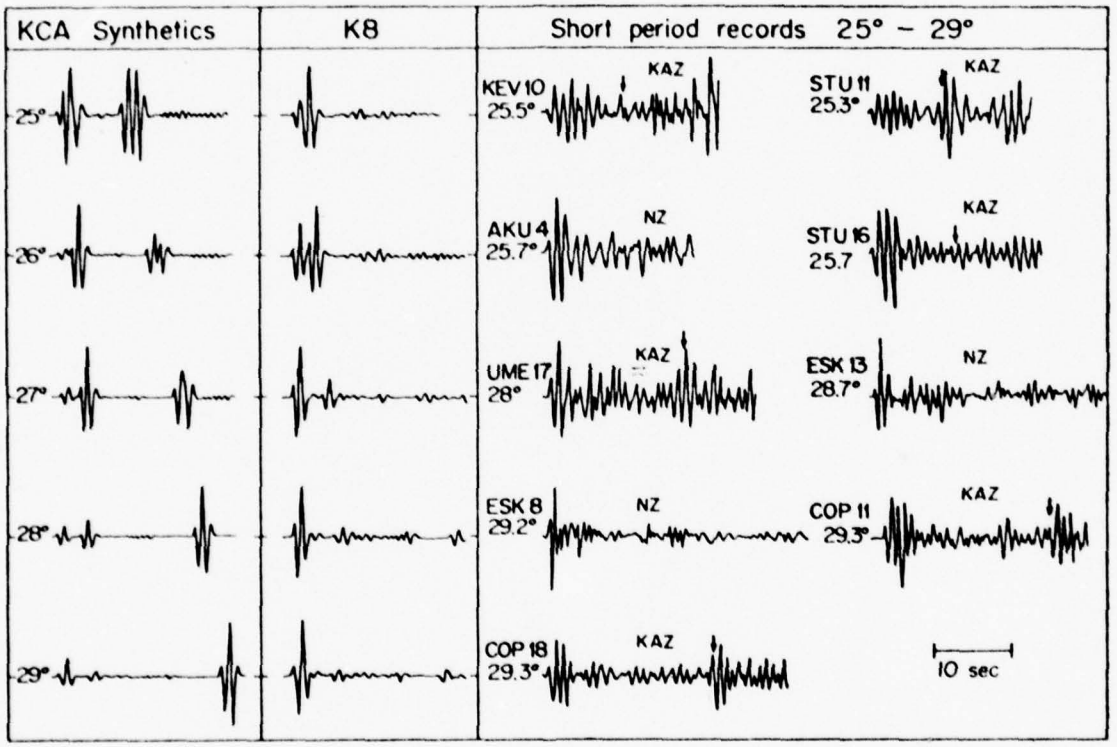
KCA Synthetics
K8
Short period records 25° – 29°
25°
26°
27°
28°
29°
KEV 10
25.5°
KAZ
STU 11
25.3°
KAZ
AKU 4
25.7°
NZ
STU 16
25.7
KAZ
UME 17
28°
KAZ
ESK 13
28.7°
NZ
ESK 8
29.2°
NZ
COP 11
29.3°
KAZ
COP 18
29.3°
KAZ
10 sec

Fig. 13

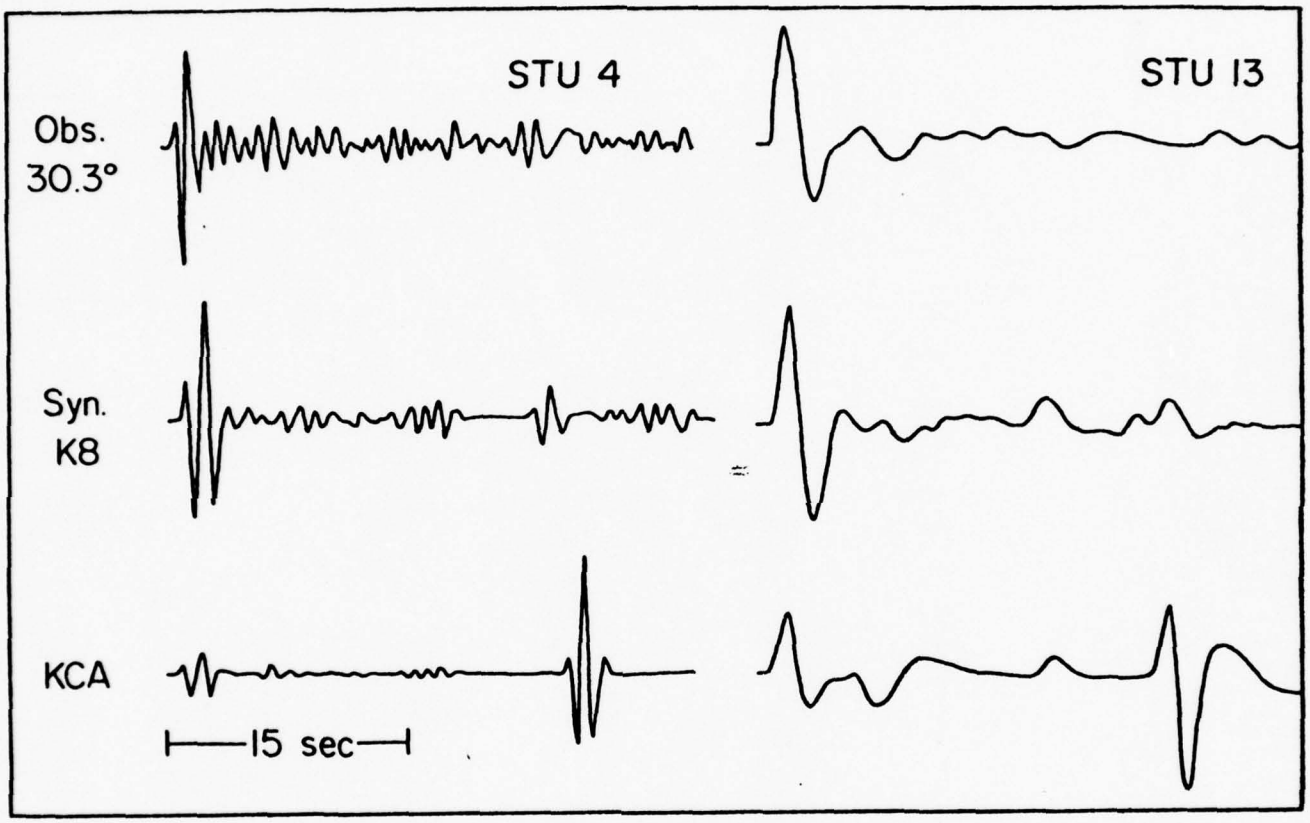

Fig. 14

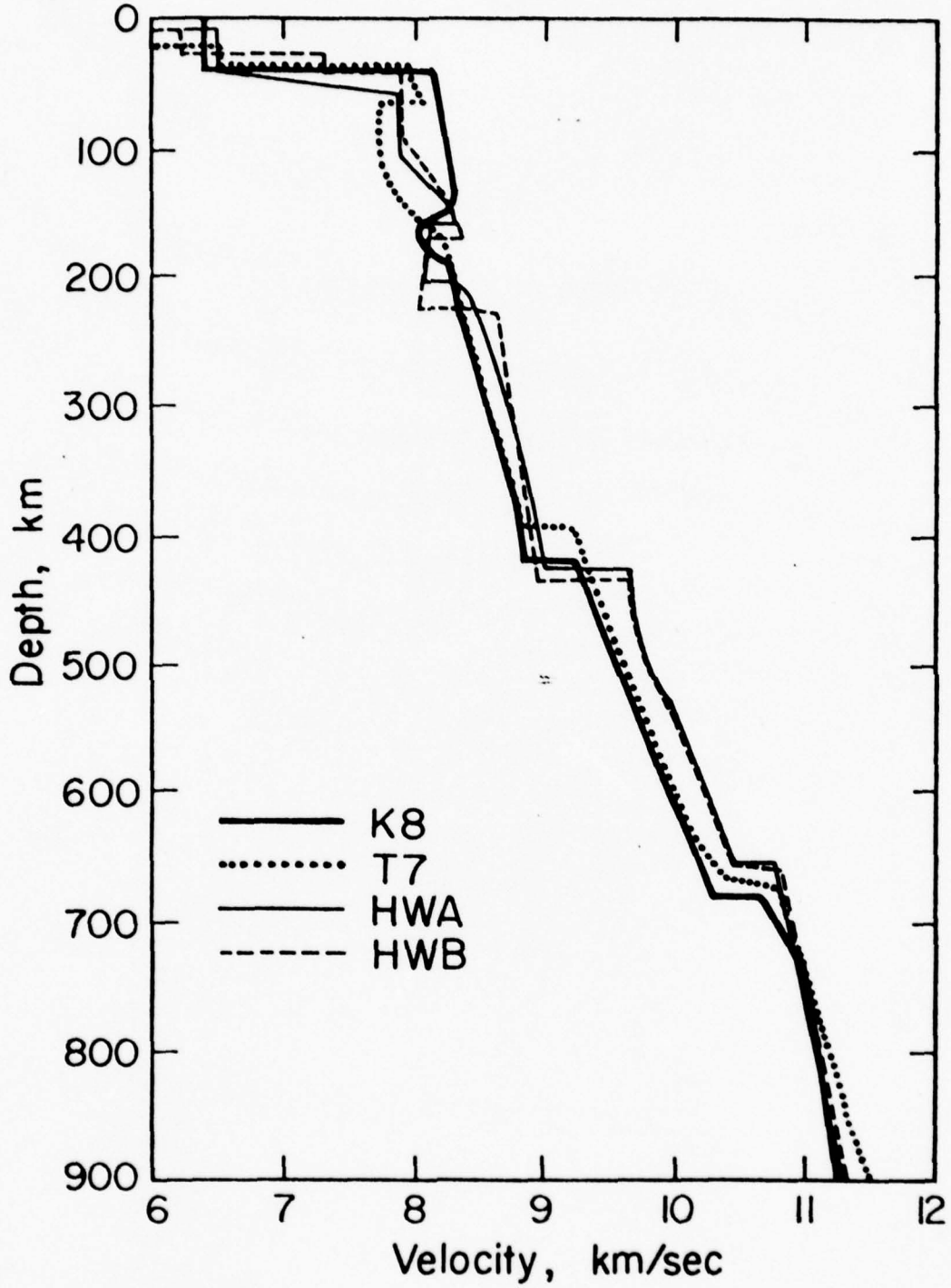
0
100
200
300
400
500
600
700
800
900
Depth, km
6
7
8
9
10
11
12
Velocity, km/sec
K8
T7
HWA
HWB

Fig. 15

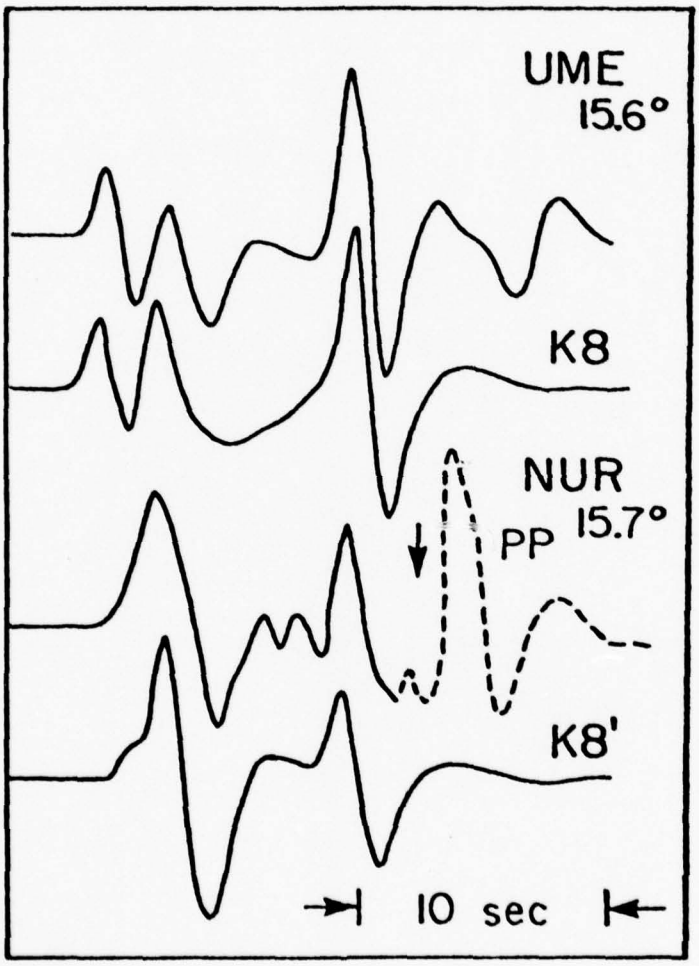

Fig. 16

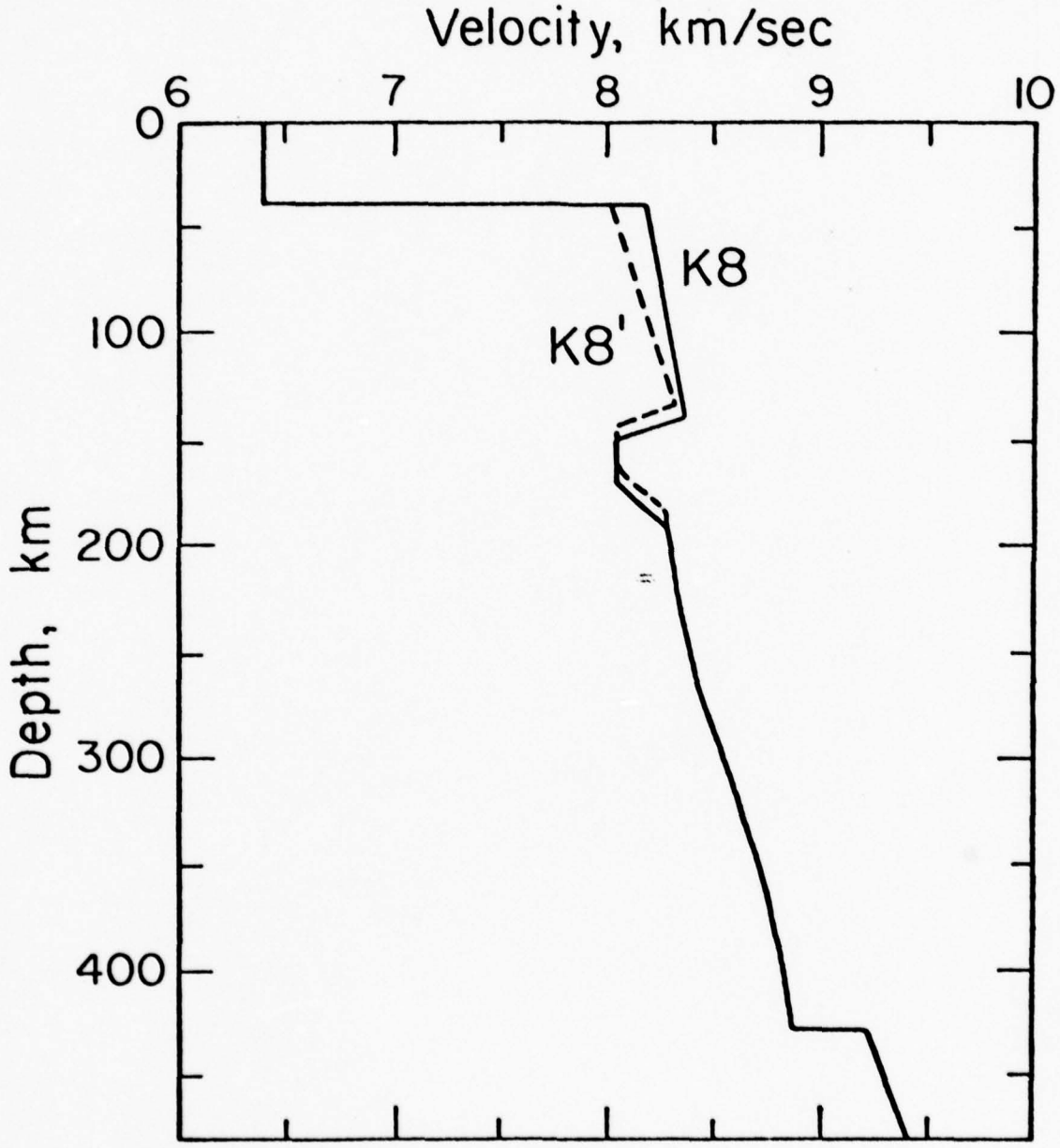

Fig. 17

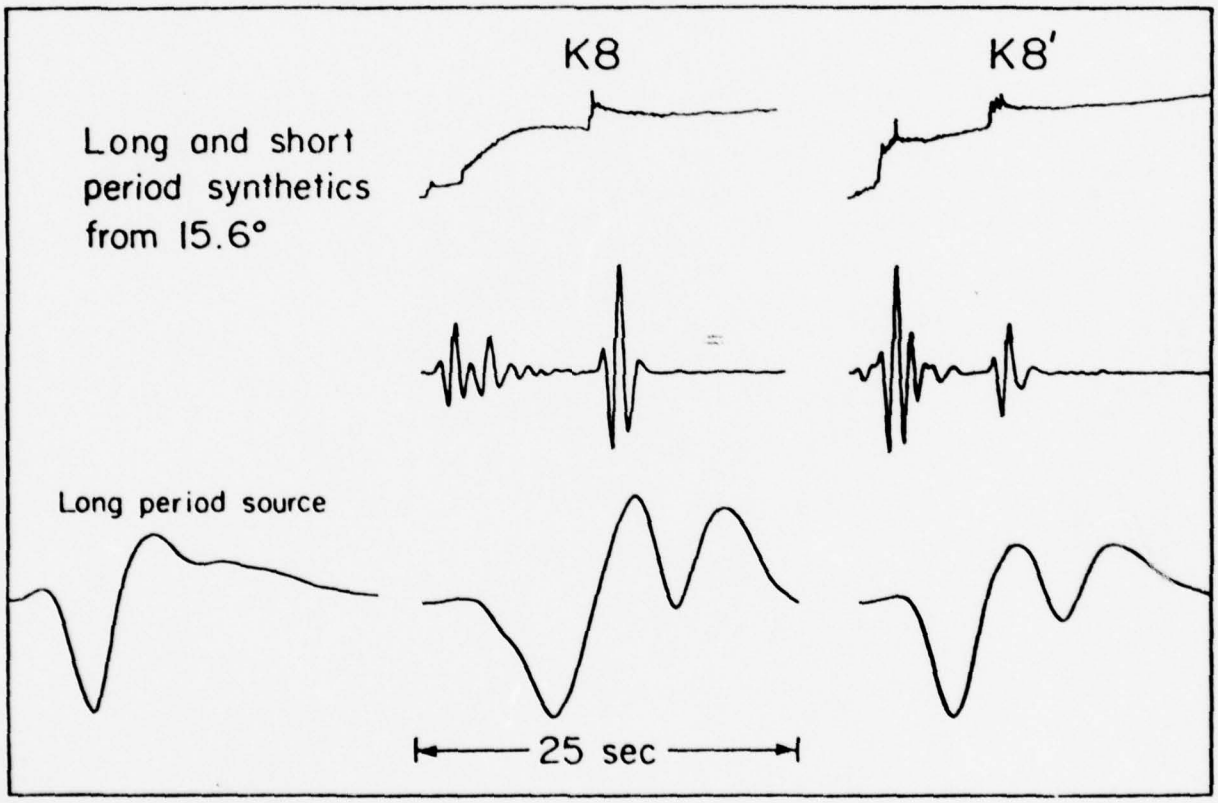
K8
K8'
Long and short
period synthetics
from 15.6°
Long period source
25 sec

Fig. 18

III. TELESEISMIC PROSPECTING OF NON-STRATIFIED RECEIVER STRUCTURES

By Tai-Lin Hong

I. INTRODUCTION

Seismic prospecting is usually conducted in two ways. The first is the method of zero-offset seismic sections. It is good for fine anomalous structures like the petroleum reservoir but is subject to shallow penetration and a narrow range of scope. The second is the method of refraction profiles. It is good for structures whose interfaces are planar but not able to find curved anomalies.

In this paper another approach using teleseismic body waves as sources is discussed. This approach has two merits. First, it can sense the structures in the depth since the wave comes steeply. Secondly, since the incident wavefront is planar, the resultant wave forms in the receiver structure have the minimum feature of dispersion; therefore, the high-frequency approximations can be used to recover the information contained in the wave forms.

As a matter of fact, this approach has been discussed for the cases of planar structures by Burdick and Langston (1977) and Langston (1977) among others. Therefore, this paper will stress on the structures with curved boundaries.

II. THE PATH OF MULTIPLE BOUNCES IN THREE-DIMENSIONAL STRUCTURES

In a three-dimensional structure, a ray can be bent to a quite different azimuthal direction after several bounces. This effect is sensitive to the structure geometry as well as the incident direction and results in various waveform distortions.

In this section we will illustrate this effect through several cases in which the structures are of the type of a sedimentary basin over a half-space. The S-velocity, P-velocity, and density of the material in the basin are assumed to be 0.7 km/sec, 1 km/sec, and 2 g/cm^3. Those in the half-space are assumed to be 3.5 km/sec, 5 km/sec and 3.3 g/cm^3.

The geometry of the interface can be expressed as

$$z = d + \frac{c}{2}\left[1 - \text{Cos}\ \frac{2\pi(x^2 + y^2 - w/2)}{w}\right] \qquad \text{(Eq. 1)}$$

where x, y, and z are the coordinates in a master frame, as shown in in Fig. 1-a.

c and d are the parameters related to the thickness of the basin

w is the parameter related to the width of the basin; it is a function of x and y as follows

$$w = w_o \frac{x^2 + y^2}{(1-A^2)\ x^2 + y^2} .$$

The incident direction of the plane wave is expressed in terms of the azimuth ϕ_o and latitude θ_o in the master frame as follows:

$$\hat{v} = (v_x, v_y, v_z) = (\sin\theta_o\cos\phi_o,\ \sin\theta_o\sin\phi_o,\ \cos\theta_o).$$

For the convenience of the scanning procedure which will be illustrated in the next section, we need a scanning frame x'- y'-z'. A

reference point (x_o, y_o, z_o) is set somewhere below the receiver structure. The scanning frame is formed by translating the master frame to (x_o, y_o, z_o) and rotating it by the azimuthal angle ϕ_o and the latitude angle θ_o. Therefore, the z'-axis is parallel to the incident direction of the plane wave. Then, we pick an azimuthal direction in the scanning frame to set up a baseline along which the scanning rays are sent from the plane $z' = 0$.

In each of the following cases, we will send a group of rays of S phase along the same baseline. These rays are transmitted into the basin, reflected twice on the interface, and terminated on the surface.

Case 1

The parameters for the geometry of the interface are:

$d = -1$ km, $c = -5$ km, $w_o = 50$ km, and $A = 0$.

The incident direction of the plane wave is:

$\phi_o = 0.2$ radians, $\theta_o = 0.2$ radians.

The scanning reference point (x_o, y_o, z_o) is set at (0, 0, -20 km).

The scanning baseline is set at the azimuth 0^o in the scanning frame.

Notice that the structure here is cylindrically symmetric. Since this group of rays are sent on a plane which contains the axis of symmetric, there is no azimuthal scattering, as shown in Fig. 1-a.

Case 2

The structure and the incident direction of the plane wave are exactly the same as those in Case 1.

The scanning reference point (x_o, y_o, z_o) is set at (-5 km, -5 km, -20 km).

The scanning baseline is set at the azimuth 0^o in the scanning frame.

Now, this group of rays is no longer on a plane which contains the axis of symmetry; therefore, these rays are scattered azimuthally as shown

in Fig. 1-b. We can see from the horizontal projection that the sharpest bending of the scanning rays occurs when the rays are transmitted into the basin, because of the large velocity contrast at the interface.

Case 3

The structure is exactly the same as that in Case 1.

The incident direction of the plane wave is

ϕ_o = 1.5708 radian, θ_o = 0.2 radian.

In other words, the plane wave is propagating upward along the z-axis and forward along the y-axis.

The scanning reference point (x_o, y_o, z_o) is set at (0, 0, -20 km).

The scanning baseline is set at the azimuth -1.5708 radian in the scanning frame. From the horizontal projection, we can see that the rays, advancing in the y-direction, are turning around after the transmission. At the edge of the basin, the horizontal projections of the ray segments in the basin are very short because of their steep paths.

Case 4

In this case, everything except the geometry of the interface is the same as that in Case 1.

The parameters for the geometry of the interface are:

d = -1 km, c = -5 km, w_o = 50 km, A = 0.5.

The contours of this interface are elliptical as shown in Fig. 1-a. Also, notice that the cross section of this basin on the plane y = 0 is wider than those in the previous cases.

III. THE SCANNING PROCEDURE

Because a multiple bounce often varies its azimuthal direction along its path, it is not trivial to predict the starting azimuth for a geometric ray leading to a given receiver location. A scanning procedure is suggested. The trial rays are sent in systematic ways to find the approximate direction of a geometric path. Then, we can take a fine tuning procedure to obtain the required accuracy.

In this section we will illustrate the scanning procedure for a case in which the structure is of the type of a two-dimensional sedimentary basin over a half-space. The materials in the basin and in the half-space are the same as those in the cases of Section II. The analytical representation of the geometry of the interface is as follows:

$$z = d + \frac{c}{2}\left[1 - \text{Cos}\ \frac{2\pi(x - w/2)}{w}\right] \qquad \text{(Eq. 2)}$$

where x, z are the cordinates shown

d and c are the parameters related to the thickness of the basin

w is the parameter related to the width of the basin.

In this case, d, c, and w are assumed to be -1 km, -5 km, and 50 km, respectively.

The incident direction of the plane wave is:

$\phi_o = 1.5708$, $\theta = 0.31416$ radians.

Notice that this plane wave is propagating not only upward along the z-axis but also forward along the y-axis. Therefore, although the structure geometry is not varying along the y-axis, this incident direction makes this problem actually a three-dimensional problem.

The scanning reference point (x_o, y_o, z_o) is set at (0, 0, -20 km).

In Fig. 2 are shown the horizontal projections of eight groups of scanning rays. They are plotted in Fig. 2-a through 2-h. The azimuth angle of the baseline of each group in the scanning frame is -2.0416, -1.7916, -1.5416, -1.0416, -0.3, -0.2, -0.1, 0 radians, respectively.

The scanning rays illustrated here are all in S mode. They are transmitted into the basin, reflected four times on the interface, and terminated on the surface.

In Fig. 2-a through 2-d, the patterns of azimuthal scattering are similar. The projections of the ray segments in the half-space are neatly lined up. The paths of the first ray segments in the basin are very steep because of the large velocity contrast. Thus their horizontal projections are very short. The ray segments in the layer tend to propagate along the x-direction since the interface is curved along that direction.

In Fig. 2-e through 2-g, we can see more clearly how these ray segments in the basin are bouncing back and forth near the cental region of the basin.

By tracking the location where each of these scanning rays terminates, we can eventually find a ray tube containing the receiver for the following procedure of fine tuning.

IV. WAVE FORM SYNTHESIS

The glorified optics (see Hong and Helmberger, 1978; and Hong, 1979) is used to synthesize the wave forms. It is a high frequency approximation. The reflection-transmission effects are evaluated in every local frame formed by the normal and tangential plane to a boundary. The spreading effects are evaluated globally through infinitesimal ray tubes. The displacement, $\underset{\sim}{u}$, can be simply written as follows:

$$\underset{\sim}{u} = \sum_{n=1}^{N} \left\{ f(t - t_o)\ \mathrm{Re}(\mathcal{S}\underset{\sim}{\mathcal{J}}) + f^*(t - t_o)\ \mathrm{Im}(\mathcal{S}\underset{\sim}{\mathcal{J}}) \right\}_n \qquad \text{(Eq. 3)}$$

where N is the total number of rays considered

t_o is the traveling time of each ray from the baseline to the receiver

$\mathcal{S}$ is the spreading effect

$\underset{\sim}{\mathcal{J}}$ includes the strength of the potential field of the incident plane wave, the reflection-transmission effect, and the receiver response

f is the convolution of the source time function and the instrument response

f* is the Hilbert transformation of f

For evaluating $\mathcal{S}$, we send a cylindrical ray tube from the plane $z' = 0$ in the scanning frame, we take the square root of the ratio of its cross section in the half-space to the projected cross section at the receiver, and determine the 90^o phase shift by inspecting the rotation of the element rays of the tube. The ray tube is supposed to be infinitesimal; the limiting procedure is taken numerically.

For evaluating $\underline{J}$, we first find the potential vector $\underline{\psi}$ for the incident S wave or the scalar potential ϕ for the incident P wave, and transfer it in local frames to obtain the transmitted or reflected potentials. The potential field reaching the receiver is converted to the displacement field.

A more detailed description of the glorified optics for three-dimensional problems can be found in Hong's (1979) paper.

The nature of wave-form complication in some two-dimensional structures has been discussed in Hong and Helmberger's paper (1978). Now, we like to see, from a case of a two-dimensional structure to a case of a three-dimensional structure, what kinds of further complications can be added to the wave forms. Briefly speaking, they can be attributed to two reasons. First, there are more rays arriving from various azimuthal directions. This can be easily conceived by looking at Fig. 1. Secondly, the spreading effect is sensitive to the curvature in azimuthal directions. To illustrate this, we consider a two-dimensional structure like that in the case of Section III and a three-dimensional structure like that in Case 1 of Section II. In each case we examine a ray tube surrounding the geometric path of a multiple bounce which is transmitted into the basin, reflected three times on the interface, and terminated at the receiver (16 km, 0, 0). The vertical projections and horizontal projections of these ray tubes are almost identical. But the horizontal projections show the difference. We notice that the ray tube in the three-dimensional structures is twisted. Such ray tubes of large size are just used for the purpose of illustration. For computing the spreading effect, much finer tubes should be used.

In the remaining part of this section, we will synthesize and compare the displacement wave forms for three groups of cases to show how much the wave forms can be sensitive to the azimuthal variation of the geometry of a structure. Ricker's wavelets are used as f(t), i.e.,

$$f(t) = \frac{\pi}{2}\,(a - \frac{1}{2})e^{-a}, \qquad \text{(Eq. 4)}$$

where

$$a = \frac{(t - Tp)^2}{(Tp\ \frac{1}{\pi})^2}$$

In each of the following cases, we use two f(t)'s with Tp equal to 18.3 sec and 3 sec, respectively. Notice that the difference between the long period response and the short period response is mainly due to the traveling time of each arrival instead of the intrinsic frequency dependence. The latter is at most 90^o phase shift in the high frequency approximation.

1) Group A

In this group we will compare the responses of a two-dimensional and a three-dimensional structure to the same incident S plane wave. The structures are of the type of a sedimentary basin over a half-space. The material structure is the same as that described in Section II. The incident direction of the plane wave is assumed to be vertical. The displacement field $\underset{\sim}{u}^o$ of the incident wave is assumed to be:

$$\underset{\sim}{u}^o = (u_x^o\ ,\ u_y^o,\ u_z^o) = (0,\ 1,\ 0).$$

Case 1

The structure is two-dimensional. The representation form for the geometry of the interface is (Eq. 2) with the following parameters:

$d = -1$ km, $c = -5$ km, $w_o = 50$ km.

Its cross section on the plane $y = 0$ and its contours are plotted in Fig. 4. The receiver location (x, y, z) is assumed to be $(0., 0., 0.,)$. The scanning reference point (x_o, y_o, z_o) is set at $(0, 0, -20$ km$)$. The traveling time, $\mathcal{S}$, and $\underset{\sim}{\mathcal{J}}$ of each arrival are listed in Table 1. The displacement wave forms are plotted in Fig. 5-a.

Case 2

The structure is three-dimensional. The analytical representation of the geometry of the interface is of the following form,

$$z = d + \frac{c}{2}\left[1 - \cos\frac{2\pi(x^2 + y^2 - w/2)}{w}\right] \qquad \text{(Eq. 5)}$$

where

$$w = w_o \frac{(x^2 + y^2)}{x^2 + (1-A^2)y^2} .$$

The parameters are assumed as follows:

$d = -1$ km, $c = -5$ km, $w_o = 50$ km, $A = 0.5$.

Its cross section on the plane $y = 0$ and its contours are plotted in Fig. 6. The receiver and the scanning reference point are the same as those in the last case.

The traveling time, $\mathcal{S}$, and $\underset{\sim}{\mathcal{J}}$ of each arrival are listed in Table 2. By comparing the rays No. 1 to 11 in Table 1 and those in Table 2, we can see these rays are taking the same geometric path in the two structures, but their spreading effects are different. We can see the higher concentrations in the three-dimensional structure. Also, we notice that in the three-dimensional structure there are more rays which are propagating on the plane $x = 0$. Those rays are listed in Table 2 as

rays No. 12 to 17. However, their contribution to the wave-form distribution is slight. The reason is that those rays are reflected as SV waves in the local frames and thus lose more energy than if they were local SH waves.

The displacement wave forms of this case are plotted in Fig. 5-b.

ii) Group B

In Case 2 of the last group, the rays No. 12 to No. 17 do not contribute to the wave-form distortion significantly. Now, assume the rays are in P mode; those rays will then become relatively important. To make the problem simpler, we assume the materials are fluid. The P-velocity and density are assumed to be 0.7 km/sec and 2 g/cm^3 in the basin and to be 3.5 km/sec and 3.3 g/cm^3 in the half-space. The plane wave is assumed to be vertically incident with the displacement field x_o as follows,

$$\underset{\sim}{u}^o = (u_x^o, u_y^o, u_z^o) = (0, 0, 1).$$

Here follow Case 3 and Case 4, corresponding to Case 1 and Case 2, respectively.

Case 3

The structure geometry, the receiver location, and the scanning reference point are the same as those in Case 1. The arriving time, $\mathcal{S}$, and $\underset{\sim}{\mathcal{I}}$ are listed in Table 3. The displacement wave forms are plotted in Fig. 5-c.

Case 4

The structure geometry, the receiver location, and the scanning reference point are the same as those in Case 2. The traveling time, $\mathcal{S}$, and $\underset{\sim}{\mathcal{I}}$ are listed in Table 4. The displacement wave forms are plotted in Fig. 5-d.

Now, we can see from Fig. 5-d that rays No. 12 and No. 13, which are propagating on the plane x = 0, result in a large spike which does not appear in Fig. 5-c.

iii) Group C

In this group we will examine the response of a two-dimensional structure to the plane waves incident in different azimuthal directions. The structure used in this group is the same as that in Case 1 of this section.

Case 5

The incident direction of the plane S wave is

$\phi_o = 0$, $\theta = 0.31416$ radians.

Its displacement field is $\underset{\sim}{u}^o = (u_x^o, u_y^o, u_z^o) = (0, 1, 0)$.

The receiver location (x, y, z) is set at (0, 0, 0).

The scanning reference point (x_o, y_o, z_o) is set at (0, 0, -20 km).

Notice that the geometric ray paths are all on the plane y = 0. The rays are all SH waves in local frames. The effects of the concentration and triplication are similar to those discussed in the previous cases of two-dimensional structures. The traveling time, $\mathcal{S}$, and $\underset{\sim}{\mathcal{J}}$ of each arrival are listed in Table 5. The displacement wave forms are plotted in Fig. 5-e.

Case 6

The incident direction of the plane S wave is

$\phi_o = 1.5708$ radians, $\theta_o = 0.31416$ radians.

The displacement field $\underset{\sim}{u}^o$ of the incident wave is

$$\underset{\sim}{u}^o = (u_x^o, u_y^o, u_z^o) = (1, 0, 0).$$

The locations of the receiver and the scanning reference point are the same as those in the last case.

Notice that the geometric ray paths are all on the plane x = 0. The rays are all SH waves in local frames. There is no triplication because the cross section of the structure on the plane x = 0 is flat. However, the effects of concentration and phase shift, caused by the curvature of the interface, are obviously showing up in Fig. 5-f. The traveling time, $\mathcal{S}$, and $\underset{\sim}{\mathcal{J}}$ of each arrival are listed in Table 6.

V. SEISMIC IMAGE OF A STRUCTURE PRODUCED BY AN INCIDENT PLANE WAVE

There are many parameters contributing to the wave-form distortion in a receiver structure. It is very difficult, if not impossible, to resolve the effect caused by each of those parameters from the record at a single station. However, if we are running a seismic array in a receiver region, there could be enough constraints in the data to uniquely conclude some features of the structure.

For this purpose we developed a scheme to simultaneously synthesize the wave form at each station of an array. According to the horizontal locations of those stations, the seismograms are lined up to simulate the vertical cross sections of the receiver structures. Such an assembly is called a synthesized seismic image of a structure.

Here we like to take some two-dimensional structures as examples to show how efficiently the seismic images can characterize the subsurficial structures. These structures are of the type of a soft layer over a half-space with a curved interface. The material structure in each example is assumed to be the same as that in the cases of Section II. Also, we assume the incident direction of the plane wave in each example is consistent with the two-dimensional feature of the structure. In order to make the illustration simpler, we will consider only the direct ray and the first two multiple bounces.

i) Example 1

The structure is the same as that in Case 1 of Section IV. The direction and the displacement field $\underset{\sim}{u}_o$ of the incident plane S wave are also the same as those in Case 1 of Section IV.

The receivers are distributed uniformly on the surface along the x-axis with the interval of 1 km.

The Ricker's wavelet with Tp equal to 3 sec (see Eq. 4) is used as f(t).

In Fig. 7-a is shown the synthesized seismic image produced by the vertically incident plane S wave. The part of the image produced by the direct rays gives straightforward indications about the structure. Suppose this image is a recorded one instead of a synthesized one; the following procedure is suggested to invert the structure.

First, construct a primary structure model based on the part of the image produced by direct rays, and make a synthesized image for this model to compare with the observed image. The multiple bounces then provide the clues for refining or modifying the current model. This procedure is repeated until consistency is obtained.

ii) Example 2

The only difference between this example and the last example is the incident direction of the plane S wave, which is now,

$\phi_o = 0^o$, $\theta_o = 30^o$

The seismic image is plotted in Fig. 7-b. Because the incident wave is slanting, the image of the structure is tilted as expected. The characteristics of this image actually is very similar to that of the last example. For instance, the triplication feature of the second multiple in each case appears in a similar way.

iii) Example 3

The only difference between this example and the last example is the geometry of the interface. In this example, the representation of the interface is of the form of (Eq. 2) with the following parameters,

d =-6 km, c = 5 km, w = 50 km.

Notice in this case that the layer is thin in the central part and becomes thick and flat at the edges.

The seismic image is plotted in Fig. 7-c. By comparing Fig. 7-b and 7-c, we can see the images, especially the parts produced by multiples, are strongly revealing the difference between the two structures. Their characteristic patterns are certainly clues for identifying the features of the subsurficial geometry.

VI. DISCUSSION AND CONCLUSIONS

In a receiver structure involving curved boundaries, the wave-form complications are mainly due to the concentration and triplication of the multiple bounces. From the case of a one-dimensional structure to the case of a two-dimensional structure, the variation of the wave forms is very apparent. However, from the already complicated case of a two-dimensional structure to the case of a three-dimensional structure, the further complications are existing delicately in the coda, as shown in Case 1 and 2 of Section IV. As we can see, it is rather hard to make a starting model for inverting a 3-dimensional structure if there is only a single station in the receiver region.

To practice the teleseismic prospecting efficiently, we need seismic arrays. As shown in Section V, we have developed a scheme to synthesize the seismic images, in which the direct rays associated with multiple bounces can strongly characterize the subsurficial features of the receiver structures. The scanning procedure costs just about the same in the case of a single station and in the case of one hundred stations. Of course, the fine tuning procedures certainly make the latter more expensive.

On the other hand, the accuracy is also depending on the fine tuning procedures. However, this scheme is designed to allow the sacrifice of accuracy in exchange for the computing cost. Actually, the wave forms shown in Section V were synthesized with less accuracy than those in Section IV.

There are some other inaccuracies related to the caustics and the critical and post-critical reflections, since the glorified

optics is basically a high-frequency approximation. By comparing with the results of the finite element method, the accuracy is still satisfactory even when the dominant period is as long as 20 sec (see Hong and Helmberger, 1978).

With the development of the glorified optics and the scheme for synthesizing seismic images, with the plentiful earth quakes and nuclear events, and with the ever expanding and improving seismic array techniques, we believe the teleseismic prospecting is a promising tackle to obtain the precise features of structures like sedimentary basins, salt domes, geosynclines, continental shelves, subduction plates, anomalies on Moho, etc.

FIGURE CAPTIONS

Fig. 1 Each of the four cases in this figure shows the projections of the paths of multiple bounces which are started along a baseline with a given azimuth in the scanning frame. The left column shows the projections on the plane y = 0. The right column shows the projections on the plane z = 0. The dashed curves in the right column represent the contours of the interfaces.

Fig. 2 This figure shows the horizontal projections of eight groups of rays in a scanning procedure. Each group of rays is started along a baseline with a given azimuth in the scanning frame.

Fig. 3 This figure shows the projections of ray tubes in a two-dimensional structure in (a) and (b), respectively. The left column shows the projections on the plane y = 0. The right column shows the projections on the plane z = 0. The dashed curves in the right column represent the contours of the interfaces.

Fig. 4 This figure shows the geometry of a structure of the type of a two-dimensional basin over a half-space. The left plot is its cross section on the plane y = 0. The shorter dashed curves in the right plot represent the contours of the interface, which is infinitely long in the y-direction.

Fig. 5 This figure shows the displacement wave forms for the cases in Section IV. The left column shows the longer period response. The right column shows the shorter period response. The letters x, y, z are indicating which components they are.

Fig. 6 This figure shows the geometry of a structure of the type of a three-dimensional basin over a half-space. The left plot is its cross section on the plane $y = 0$. The shorter dashed curves in the right plot represent the contours of the interface.

Fig. 7 The synthesized seismic image for the examples in Section V.

REFERENCES

Aki, K., and K. L. Larner, Surface motion of a layered medium having an irregular interface due to incident plane SH waves, J. Geophys. Res., 75, No. 5, 1970.

Burdick, L. J., and C. A. Langston, Modify crustal structure through the use of converted phases in teleseismic body waveforms, Seismol. Soc. Am., Bull., 67, 677-691, 1977.

Choy, G. L., and P. G. Richard, Pulse distortion and Hilbert transformation in multiply reflected and refracted body waves, Seismol. Soc. Am., Bull., 65, No. 1, 55-70, 1975.

Helmberger, D. V., The crust-mantle transition in the Bering Sea, Seismol. Soc. Am., Bull., 58, 179-214, 1968.

Helmberger, D. V., Generalized ray theory for shear dislocations, Seismol. Soc. Am., Bull., 64, 45-64, 1974.

Hill, D. P., Phase shift and pulse distortion in body waves due to internal caustics, Seismol. Soc. Am., Bull., 64, 1733-1742, 1974.

Hong, T. L., and D. V. Helmberger, Generalized ray theory for dipping structure, Seismol. Soc. Am., Bull., 67, 995-1008, 1977.

Hong, T. L., and D. V. Helmberger, Glorified optics and wave propagation in non-planar structures, Seismol. Soc. Am., Bull., 68, No. 5, 1313-1330, 1978.

Hong, T. L., Elastic wave propagation in irregular structures, Ph.D. thesis, Calif. Inst. of Technol., Pasadena, 1978.

Hong, T. L., The generalization of the glorified optics to 3-dimensional problems (in preparation), 1979.

Langston, C. A., Corvallis, Oregon, crustal and upper mantle receiver structure from teleseismic P and S waves, Seismol. Soc. Am., Bull., 67, No. 3, 713-724, 1977.

Langston, C. A., The effect of planar dipping structure on source and receiver responses for constant ray parameter, Seismol. Soc. Am., Bull., 67, 1029-1050, 1977.

Mack, H., Nature of short-period P-wave signal variations at LASA, J. Geophys. Res., 74, No. 12, 3161-3170, 1969.

May, B. T., and F. Hron, Synthetic seismic sections of typical petroleum traps, Geophysics, 43, No. 6, 1119-1147, 1978.

Smith, S. G., A reflection profile modeling system, R. Astron. Soc., Geophys. J., 49, 723-737, 1977.

TABLE CAPTIONS

Table 1 The arriving time (T), the spreading effect ($\mathcal{S}$), and the reflection-transmission effect ($\underset{\sim}{\mathcal{T}}$) of each arrival in Case 1 of Section IV. The number of segments along the geometric path of an arrival is indicated in the second column. The mode of each arrival is also indicated there. Notice, the P-S converted phases are not considered here.

Table 2 The arriving time (T), the spreading effect ($\mathcal{S}$), and the reflection-transmission effect ($\underset{\sim}{\mathcal{T}}$) of each arrival in Case 2 of Section IV.

Table 3 The arriving time (T), the spreading effect ($\mathcal{S}$), and the reflection-transmission effect ($\underset{\sim}{\mathcal{T}}$) of each arrival in Case 3 of Section IV.

Table 4 The arriving time (T), the spreading effect ($\mathcal{S}$), and the reflection-transmission effect ($\underset{\sim}{\mathcal{T}}$) of each arrival in Case 4 of Section IV.

Table 5 The arriving time (T), the spreading effect ($\mathcal{S}$), and the reflection transmission effect ($\underset{\sim}{\mathcal{T}}$) of each arrival in Case 5 of Section IV.

Table 6 The arriving time (T), the spreading effect ($\mathcal{S}$), and the reflection-transmission effect ($\underset{\sim}{\mathcal{T}}$) of each arrival in Case 6 of Section IV.

No	Phase	T(sec)	S	$\underset{\sim}{J}$
1	2-S	12.571	1/0.900	(0.,3.5,0.)
2	4-S	29.714	1/0.371	(0.,-2.624,0.)
3	6-S	40.014	1/1.579	(0.,3.435-0.604i,0.)
4	6-S	46.857	i/0.816	(0.,1.967,0.)
5	6-S	40.014	1/1.580	(0.,3.435-0.604i,0.)
6	8-S	44.362	1/2.765	(0.,-3.182+1.447i,0.)
7	8-S	64.000	i/0.916	(0.,-1.475,0.)
8	8-S	44.362	1/2.770	(0.,-3.182+1.447i,0.)
9	10-S	47.743	1/3.830	(0.,1.934-0.521i,0.)
10	10-S	81.143	i/0.465	(0.,1.106,0.)
11	10-S	47.743	1/3.845	(0.,1.934-0.521i,0.)

Table 1

No	Phase	T(sec)	$\mathcal{S}$	$\underset{\sim}{\mathcal{I}}$
1	2-S	12.571	1/0.852	(0.,3.5,0.)
2	4-S	29.714	1/0.261	(0.,-2.624,0.)
3	6-S	40.014	1/1.082	(0.,3.435−0.604i,0.)
4	6-S	46.857	-1/0.356	(0.,1.967,0.)
5	6-S	40.014	1/1.082	(0.,3.435−0.604i,0.)
6	8-S	44.362	1/1.903	(0.,-3.182+1.447i,0.)
7	8-S	64.000	-1/0.799	(0.,-1.475,0.)
8	8-S	44.362	1/1.907	(0.,-3.182+1.447i,0.)
9	10-S	47.743	1/2.633	(0.,1.934−0.521i,0.)
10	10-S	81.143	-1/0.462	(0.,1.106,0.)
11	10-S	47.743	1/2.644	(0.,1.934−0.521i,0.)
12	6-S	45.781	i/0.429	(0.,-0.0165−0.315i,-0.679+0.0356i)
13	6-S	45.781	i/0.429	(0.,-0.0165−0.315i,0.679−0.0356i)
14	8-S	52.672	i/1.245	$(0.,0.643+0.433i,0.639-0.949i)\times10^{-2}$
15	8-S	52.673	i/1.245	$(0.,0.643+0.433i,-0.639+0.949i)\times10^{-2}$
16	10-S	56.908	i/1.921	$(0.,-0.217-0.110i,-0.160+0.316i)\times10^{-1}$
17	10-S	56.908	i/1.921	$(0.,-0.217-0.110i,0.160-0.316i)\times10^{-1}$

Table 2

No	Phase	T(sec)	S	$\underset{\sim}{q}$
1	2-P	12.571	1/0.900	(0.,0.,+1.)
2	4-P	29.714	1/0.371	(0.,0,-0.750)
3	6-P	40.014	1/1.579	(0.,0,-0.158+0.202i)
4	6-P	46.857	i/0.816	(0. ,0.,+0.562)
5	6-P	40.014	1/1.580	(0.,0,-0.158+0.202i)
6	8-P	44.362	1/2.765	(0.,0.,+0.174-0.018i)
7	8-P	64.000	i/0.916	(0.,0,-0.421)
8	8-P	44.362	1/2.770	(0.,0.,+0.174-0.018i)
9	10-P	47.743	1/3.830	(0.,0.,-0.125-0.043i)
10	10-P	81.143	i/0.465	(0.,0.,+0.316)
11	10-P	47.743	1/3.845	(0.,0,-0.125-0.043i)

Table 3

No	Phase	T(sec)	S	$\underline{\underline{Q}}$
1	2-P	12.571	1/0.852	(0.,0.,1.)
2	4-P	29.714	1/0.261	(0.,0,-0.750)
3	6-P	40.014	1/1.082	(0.,0,-0.158+0.202i)
4	6-P	46.857	-1/0.356	(0.,0., 0.562)
5	6-P	40.014	1/1.082	(0.,0,-0.158+0.202i)
6	8-P	44.362	1/1.903	(0.,0., 0.174-0.018i)
7	8-P	64.000	-1/0.799	(0.,0,-0.421)
8	8-P	44.362	1/1.907	(0.,0., 0.174-0.018i)
9	10-P	47.743	1/2.633	(0.,0,-0.125-0.043i)
10	10-P	81.143	-1/0.462	(0.,0., 0.316)
11	10-P	47.743	1/2.644	(0.,0,-0.125-0.043i)
12	6-P	45.781	i/0.429	(0.,0,-0.093+0.572i)
13	6-P	45.781	i/0.429	(0.,0,-0.093+0.572i)
14	8-P	52.672	i/1.245	(0.,0., 0.235+0.013i)
15	8-P	52.673	i/1.245	(0.,0., 0.235+0.013i)
16	10-P	56.908	i/1.921	(0.,0 -0.130-0.118i)
17	10-P	56.908	i/1.921	(0.,0 -0.130-0.118i)

Table 4

No	Phase	T(sec)	S	$\underset{\sim}{T}$
1	2-S	12.355	1/0.899	(0.,3.626,0.)
2	4-S	29.290	1/0.447	(0.,-3.361+0.867i,0.)
3	6-S	38.134	1/1.699	(0.,3.387-0.538i,0.)
4	6-S	46.690	i/0.813	(0.,2.022,0.)
5	6-S	41.324	1/1.469	(0.,3.823-0.746i,0.)
6	8-S	42.211	1/2.861	(0.,-3.309+1.194i,0.)
7	8-S	63.788	i/0.916	(0.,-1.496,0.)
8	8-S	45.953	1/2.686	(0.,-3.118+2.170i,0.)
9	10-S	45.464	1/3.914	(0.,1.925-3.003i,0.)
10	10-S	80.804	i/0.560	(0.,-0.423-0.386i,0.)
11	10-S	49.461	1/3.774	(0.,2.462-0.714i,0.)

Table 5

No	Phase	T(sec)	S	$\underset{\sim}{\mathcal{I}}$
1	2-S	12.359	1/0.899	(3.643,0.,0.)
2	4-S	29.469	1/0.364	(-2.692,0.,0.)
3	6-S	46.579	i/0.818	(1.990,0.,0.)
4	8-S	63.690	i/0.914	(-1.471,0.,0.)
5	10-S	80.800	i/0.460	(1.087,0.,0.)

Table 6

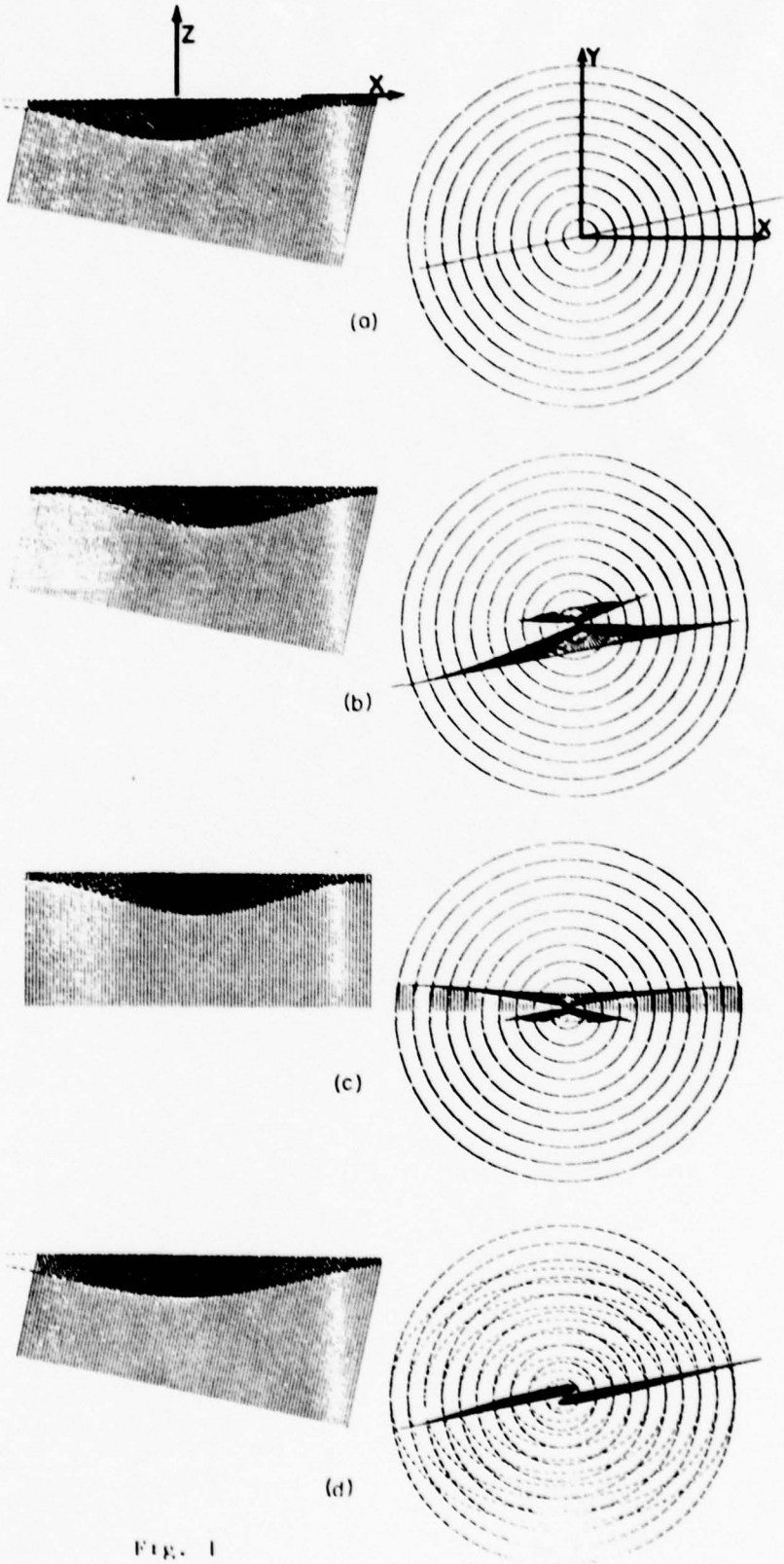

Fig. 1

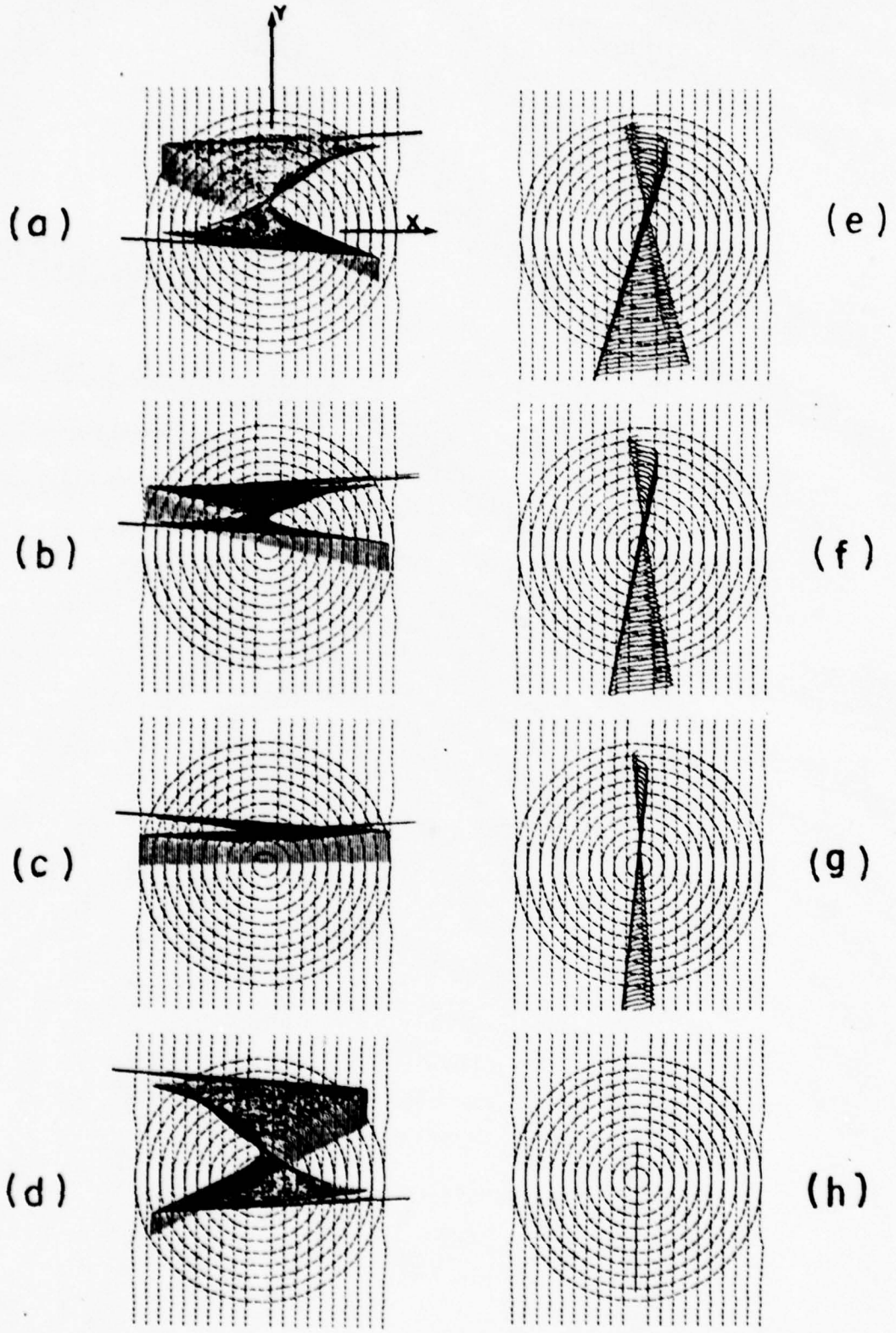

Fig. 2

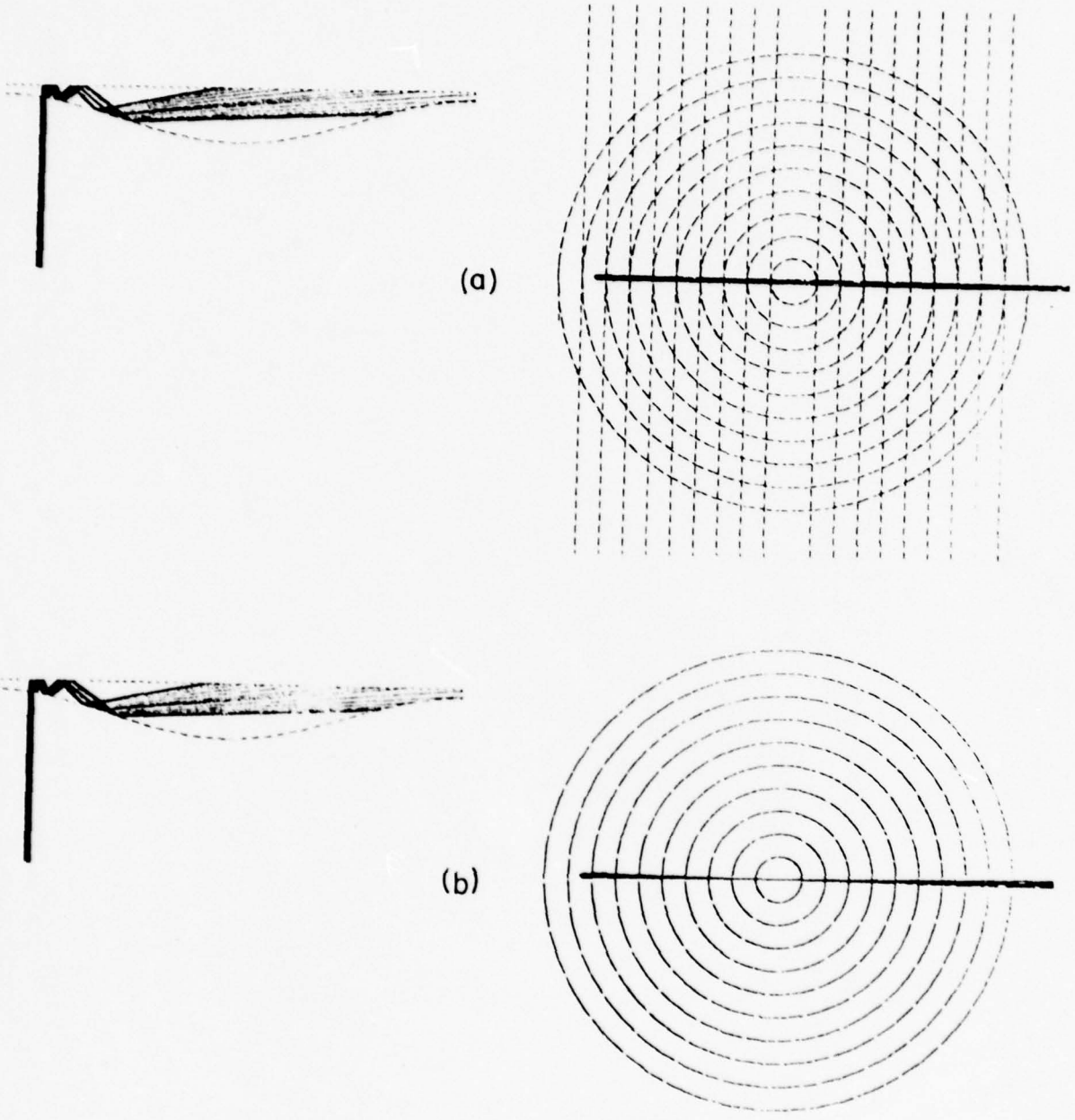

Fig. 3

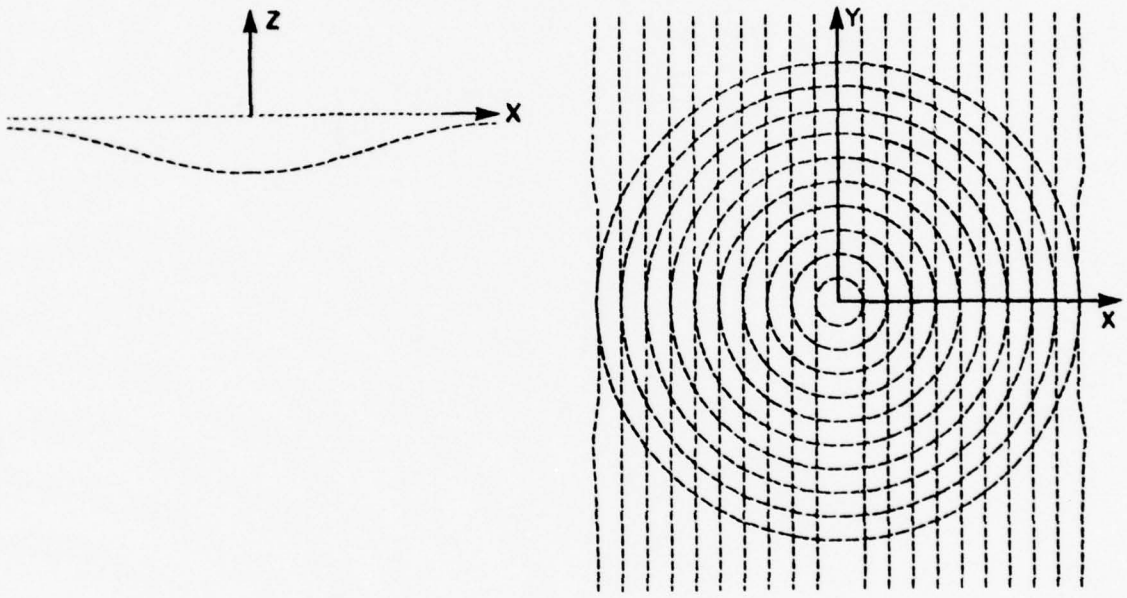

Fig. 4

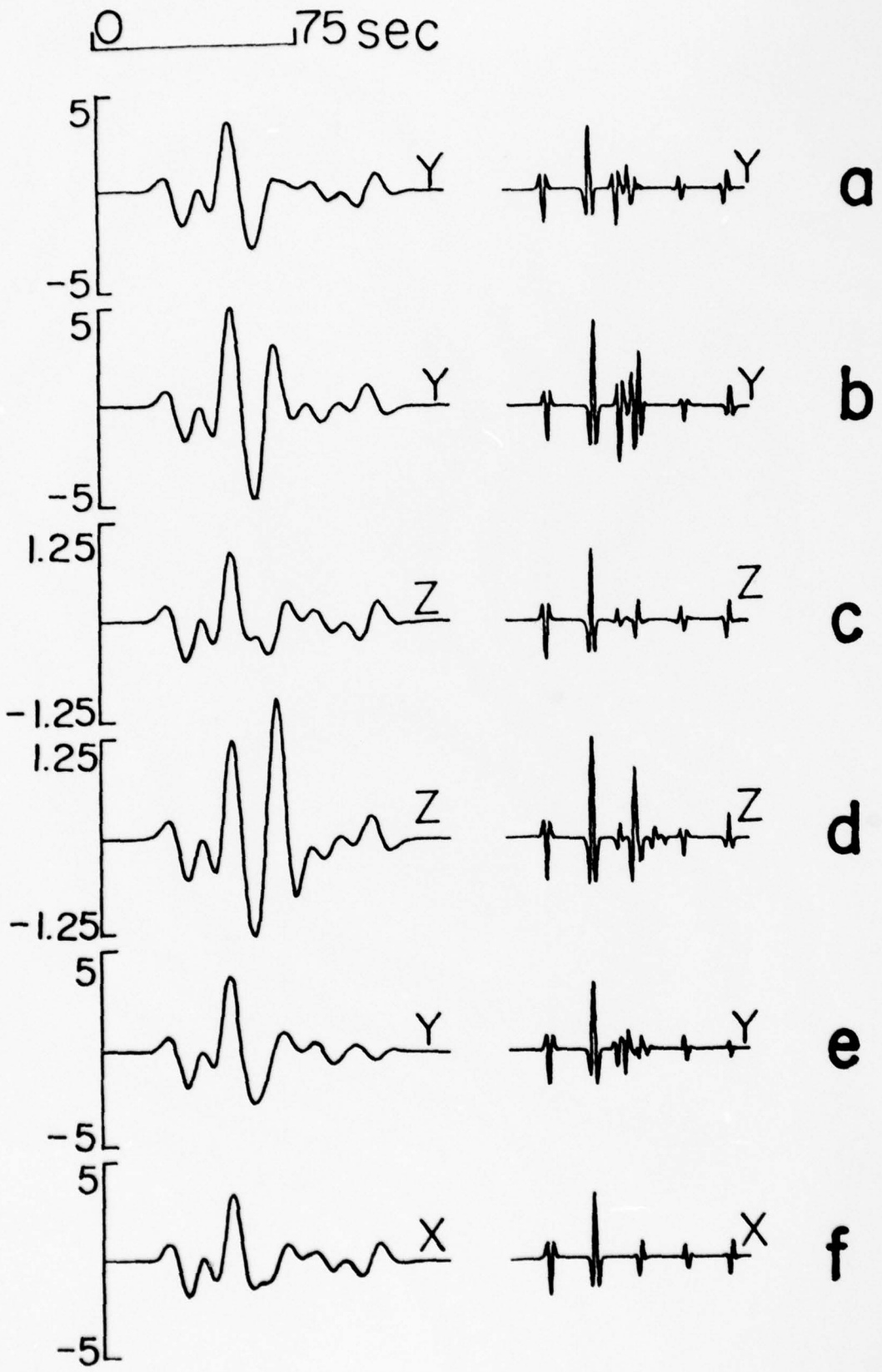

Fig. 5

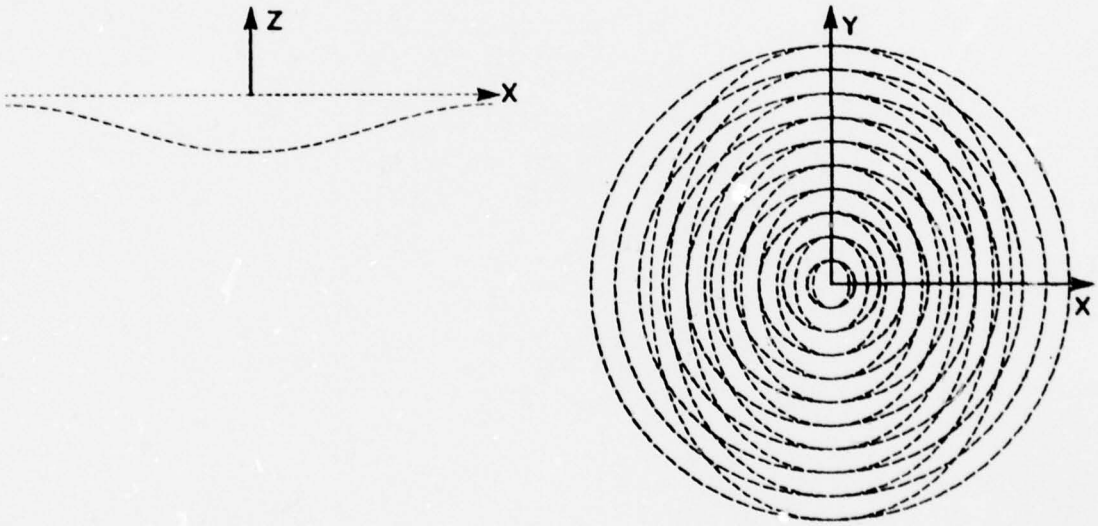

Fig. 6

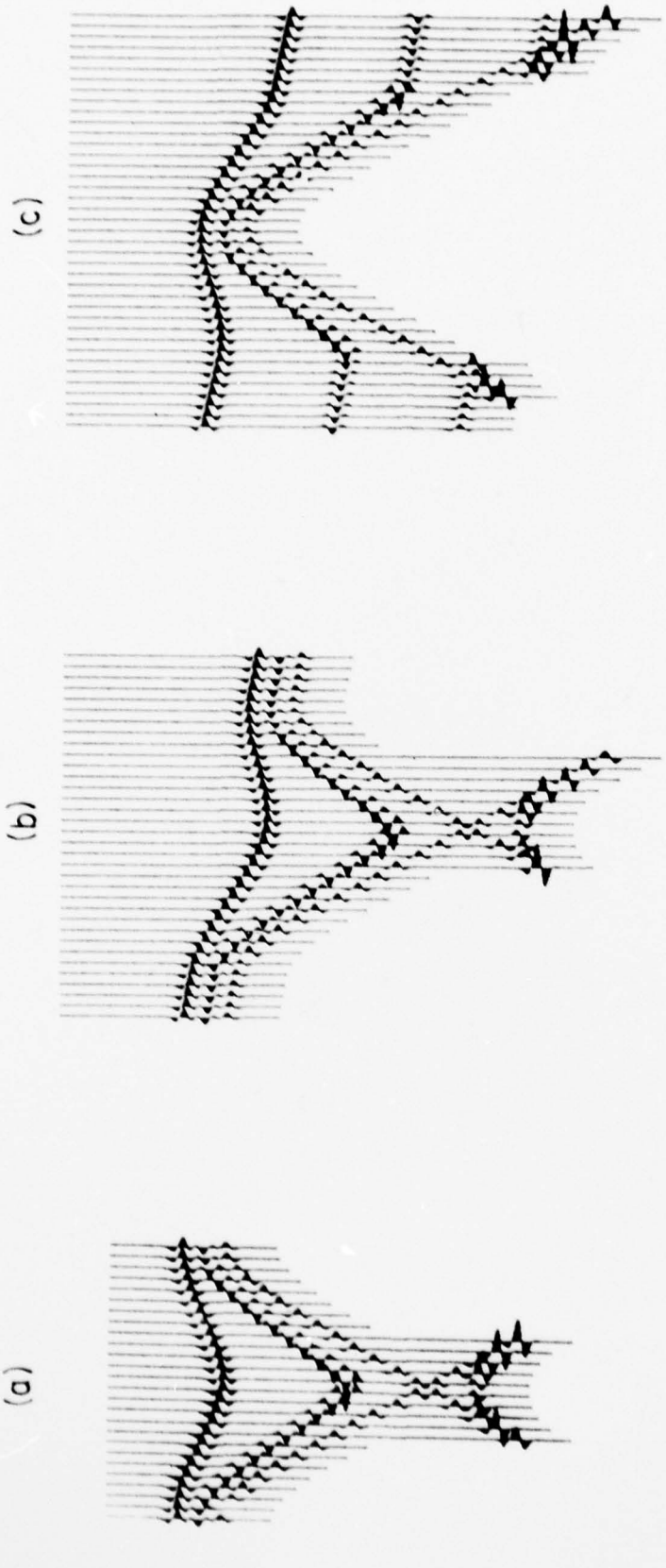

Fig. 7

IV. SLIPPING INTERFACES: A POSSIBLE SOURCE OF S RADIATION FROM EXPLOSIVE SOURCES

By Carlos Salvado and Bernard Minster

Introduction:

Considerable effort has been devoted to the understanding of SH radiation from underground explosive sources. A variety of possible mechanisms have been proposed, as reviewed by Aki and Tsai (1972). They include (1) mode conversion at irregular interfaces (e.g., Aki and Larner, 1970), (2) cracking in the vicinity of the shot point (e.g., Kisslinger et al., 1961), (3) prestress relaxation associated with the creation of the cavity (e.g., Archambeau, 1972, 1973) and (4) triggering of an actual earthquake with large scale faulting, a model favored by Aki and Tsai (1972).

It is likely that a combination of these mechanisms acts to produce the observed SH and Love wave radiation from underground explosions. The relative contributions of various mechanisms will of course depend on local characteristics of the site. Nevertheless, it may be noted that the two last mechanisms listed above involve the release of strain energy stored in the medium prior to the experiment, and therefore require the presence of sufficient prestress. On the other hand, the two first mechanisms can operate even in the absence of significant initial stress, as evidenced by the observations of Kisslinger et al. (1961). These authors observed SH radiation generated by small scale explosions detonated in mud, and suggested that near source cracking was the most likely cause of shear wave radiation.

In order to better understand the influence of site characteristics and prestress on SH and Love wave generation, an improved assessment of the phenomena which do not require prestress is needed. Cracking and block motions in the vicinity of explosions fall in this category; a review of these problems is provided by Bache and Lambert (1976).

The purpose of this paper is to demonstrate that the presence of imperfectly

bonded interfaces and joints near a purely dilational source could account for far field transverse components of displacement, and thus with a suitable geometry, for SH and Love wave radiation (e.g., Salvado and Minster, 1977). The problem is greatly simplified because we restrict ourselves to linear boundary conditions, and solve the problem in the far-field, first-motion approximation. It appears that if the bonding is sufficiently weak, and if the geometry is favorable, at least a portion of the observed shear radiation could be explained by this mechanism.

1. Statement of the Problem, and Boundary Conditions

Consider the simple geometry depicted on Figure 1: a purely dilatational point source is located at a height h above the plane interface between two elastic half spaces. To simplify the problem, we restrict our attention to the case when the two half spaces are identical. The boundary conditions usually adopted in seismology involve continuity of tractions and displacements, and in this case, the problem reduces to that of a point source in an infinite space.

We shall now relax the boundary conditions, and request continuity of tractions and of normal displacement but allow a jump in the tangentional displacement In other words, slippage is allowed between the two half spaces. Sezawa and Kanai (1940), Kanai (1961) and Murty (1975, 1976) proposed a boundary condition which does allow such slippage to occur, and has the advantage of being linear; it is best described as the result of the following limiting process.

Suppose the two half spaces are actually coupled through a viscous layer of thickness H and viscosity η. The geometry is described on Figure 2. Assuming a plane Couette flow in the viscous layer, the shear traction is related to the jump in tangential velocity by

$$\sigma_{rz} = \eta \frac{\partial \dot{u}_r}{\partial z} \cong \frac{\eta}{H} \left(\dot{u}_r(r,0^+,t) - \dot{u}_r(r,0^-,t) \right) \qquad (0 \leq \eta \leq \infty) \qquad (1\text{-}1)$$

We now allow the thickness H and the viscosity η to go to zero, but require that their ratio remain constant. For convenience in the subsequent analyses, we define

$$\frac{\eta}{H} = \frac{\Phi}{1 - \Phi} \frac{\mu}{\beta} \qquad (0 \leq \Phi \leq 1) \qquad (1\text{-}2)$$

where μ is the rigidity and β the shear wave velocity in the two half spaces.

Φ is a dimensionless bonding parameter. In this limit, the boundary condition becomes

$$\sigma_{rz} = \frac{\Phi}{1 - \Phi} \frac{\mu}{\beta} \left[\!\left[\dot{u}_r(r,0,t) \right]\!\right]_-^+ \qquad 1\text{-}3$$

where $\left[\!\left[\dot{u}_r\right]\!\right]_-^+$ is the jump of tangential velocity across the interface:

$$\left[\!\left[\dot{u}_r(r,0,t) \right]\!\right]_-^+ = \dot{u}_r(r,0^+,t) - \dot{u}_r(r,0^-,t)$$

When $\Phi = 0$, the tangential traction vanishes and the interface is perfectly lubricated; when $\Phi = 1$, no relative motion between the two half spaces is allowed and the interface is perfectly bonded.

The main advantage of the boundary conditions (1-3) is its linearity, which greatly simplifies wave propagation problems. Imperfectly bonded interfaces have been modelled using nonlinear boundary conditions (e.g., Chez et al. (1978) and Miller (1979)), but the difficulties are such that only plane waves have apparently been considered.

2. Analysis of the Problem

The wave propagation problem is amenable to a Cagniard-de Hoop treatment,

and simple closed form solutions may be found in the first motion approximation.

We consider the potential decomposition (e.g., Cagniard, 1962)

$$\left.\begin{aligned} u_r &= \frac{\partial \Phi}{\partial r} - \frac{\partial \Psi}{\partial z} \\ u_z &= \frac{\partial \Phi}{\partial z} + \frac{1}{r}\frac{\partial}{\partial r}(r\Psi) \end{aligned}\right\} \tag{2-1}$$

and the solutions of the form

$$\left.\begin{aligned} \Phi_i &= e^{st}\, x_i \\ \Psi_i &= e^{st}\, y_i \end{aligned}\right\} \qquad i = 1,2 \tag{2-2}$$

where, for $z > 0$, the source medium,

$$\left.\begin{aligned} x_1 &= \int_0^\infty e^{-\nu_\alpha |z-h|}\, J_o(kr)\, \frac{k\,dk}{\nu_\alpha} + \int_0^\infty Q_1(k) J_o(kr) e^{-\nu_\alpha z} dk \\ y_1 &= \int_0^\infty S_1(k)\, \frac{\partial}{\partial r} J_o(kr)\, e^{-\nu_\beta z} dk \end{aligned}\right\} \tag{2-3}$$

and, for $z < 0$:

$$\left.\begin{aligned} x_2 &= \int_0^\infty Q_2(k)\, J_o(kr)\, e^{\nu_\alpha z}\, dk \\ y_2 &= \int_0^\infty S_2(k)\, \frac{\partial}{\partial r} J_o(kr)\, e^{\nu_\beta z}\, dk \end{aligned}\right\} \tag{2-4}$$

Here $$\nu_\alpha = \left[k^2 + \frac{s^2}{\alpha^2}\right]^{1/2}, \quad \nu_\beta = \left[k^2 + \frac{s^2}{\beta^2}\right]^{1/2},$$

and α, β are the P and S-wave velocities respectively.

The unknown coefficients, $\{Q_i(k), S_i(k);\ i = 1,2\}$ are to be determined by use of the boundary conditions. Continuity of tractions, normal displacement,

slip condition (1-3) lead to the following system of simultaneous equations.

$$\begin{pmatrix} \nu_\alpha & \nu_\alpha & k^2 & -k^2 \\ -a & a & -2\mu\nu_\beta k^2 & -2\mu\nu_\beta k^2 \\ 2\mu\nu_\alpha & 2\mu\nu_\alpha & a & -a \\ b & -b & c & c \end{pmatrix} \begin{pmatrix} Q_1 \\ Q_2 \\ S_1 \\ S_2 \end{pmatrix} =$$

$$= m \begin{pmatrix} 1 \\ a/\nu_\alpha \\ 2\mu \\ 2\mu\left[\mu(1-\phi) - \frac{s}{\beta\nu_\alpha}\phi\right] \end{pmatrix} \qquad (2\text{-}5)$$

where

$$\left.\begin{aligned} a &= 2\mu k^2 + \rho s^2 \\ b &= 2\mu\left[(1-\phi)\nu_\alpha + \frac{s}{\beta}\phi\right] \\ c &= a(1-\phi) + \frac{2\mu s\nu_\beta}{\beta}\phi \\ m &= ke^{-\nu_\alpha h} \end{aligned}\right\} \qquad (2\text{-}6)$$

The determinant in (2-5) is given by

$$\Delta(k) = 4\rho\nu_\alpha s^2 D(k) \qquad (2\text{-}7)$$

$$D(k) = \left[(2\mu k^2 + \rho s^2)^2 - 4\mu^2\nu_\alpha\nu_\beta k^2\right](1-\phi) + \frac{2\mu\rho\nu_\beta}{\beta} s^3 \phi$$

Notice that the bracketed expression in D(k) is the Rayleigh denominator.

The solutions to (2-5) are

$$Q_1(k) = \frac{-ke^{-\nu_\alpha h}}{D(k)}\left[4\mu^2\nu_\beta k^3 (1-\phi)\right] \qquad (2\text{-}8a)$$

$$Q_2(h) = \frac{ke^{-\nu_\alpha h}}{\nu_\alpha D(k)}\left[\frac{2\mu\rho\nu_\beta}{\beta} s^3\phi + (2\mu k^2 + \rho s^2)^2 (1-\phi)\right] \qquad (2\text{-}8b)$$

$$S_1(k) = S_2(k) = \frac{k e^{-\nu_\alpha h}}{D(k)} \left[2\mu (2\mu k^2 + \rho s^2)(1-\phi) \right] \qquad (2\text{-}8c)$$

In the case of a perfectly bonded interface, $\phi = 1$, and the only nonvanishing coefficient is $Q_2(k)$, as expected.

By considering derivatives of these coefficients with respect to the bonding parameter ϕ, one finds that no extrema occur for $\phi \in]0,1[$. In other words the most efficient conversion of P waves to S waves must occur for $\phi = 0$, that is, a perfectly lubricated interface.

We can now substitute these coefficients in the solutions (2-3) and(2-4), and replace k in terms of the ray parameter p (e.g., de Hoop, 1960; Helmberger, 1974; Langston, 1976).

$$k = -i\, s\, p. \qquad (2\text{-}9)$$

After application of the Schwartz reflection principle, the solution takes the form

$$x_i = \frac{2}{\pi} \operatorname{Im} \int_0^{i\infty} Q_i(p)\, K_0(spr)\, dp \qquad (2\text{-}10a)$$

$$y_i = \frac{2}{\pi} \operatorname{Im} \int_0^{i\infty} S_i(p)\, \frac{\partial K_0(spr)}{\partial r}\, dp \qquad (2\text{-}10b)$$

where

$$Q_1(p) = \frac{e^{-sn_\alpha |z-h|}}{n_\alpha} sp - \frac{4\mu^2 (1-\phi)\, sp^3 n_\beta\, e^{-sn_\alpha |z+h|}}{D(p)} \qquad (2\text{-}11a)$$

$$Q_2(p) = \frac{e^{-sn_\alpha (h-z)}}{n_\alpha D(p)} \left\{ \frac{2\mu\rho n_\beta}{\beta} \phi + (\rho - 2\mu p^2)^2 (1-\phi) \right\} \qquad (2\text{-}11b)$$

$$S_1(p) = \frac{e^{-s(n_\alpha h + n_\beta z)}}{D(p)} 2\mu(1-\phi)\, p(\rho - 2\mu p^2) \qquad (2\text{-}11c)$$

$$S_2(p) = \frac{e^{-s(n_\alpha h - n_\beta z)}}{D(p)} 2\mu(1-\phi)\, p(\rho - 2\mu p^2) \qquad (2\text{-}11d)$$

and where the following definitions hold

$$\eta_\alpha = \left(\frac{1}{\alpha^2} - p^2\right)^{1/2}; \quad \eta_\beta = \left(\frac{1}{\beta^2} - p^2\right)^{1/2} \tag{2-12}$$

$$\mathcal{D}(p) = [(\rho - 2\mu p^2)^2 + 4\mu^2 \eta_\alpha \eta_\beta p^2] \ (1-\Phi) + \frac{2\mu\rho\eta_\beta}{\beta} \Phi \tag{2-13}$$

Asymptotic approximations of (2-10) and first motion approximations can then be obtained in the usual fashion (e.g., Langston, 1976). By substitution of the asymptotic results

$$K_o(spr) \sim \sqrt{\frac{\pi}{2spr}} \ e^{-spr}$$

$$\frac{\partial K_o(spr)}{\partial r} \sim -sp \sqrt{\frac{\pi}{2spr}} e^{-spr} \tag{2-14}$$

the solution (2-10) are reduced to integrals of the form

$$I(r,z,s) = \sqrt{\frac{2}{\pi sr}} \ \mathrm{Im} \int_o^{i\infty} e^{-st(r,z,p)} f(p) dp \tag{2-15}$$

from which the displacement must be retrieved via the formulae (2-1). This requires finding the spatial derivatives of I. Keeping only the far-field terms, we have

$$\frac{\partial I(r,z,s)}{\partial r} = -s\sqrt{\frac{2}{\pi sr}} \ \mathrm{Im} \int_o^{i\infty} e^{-st(r,z,p)} pf(p) dp \tag{2-16}$$

$$\frac{\partial I(r,z,s)}{\partial z} = -s \sqrt{\frac{2}{\pi sr}} \ \mathrm{Im} \int_o^{i\infty} e^{-st(r,z,p)} \frac{\partial t}{\partial z} f(p) dp \tag{2-17}$$

The body wave contributions, which we are interested in, are obtained by changing the variable of integration to t so that by use of Cauchys-Goursats' theorem on the complex t-plane we have

$$\frac{\partial I}{\partial r} = -s \sqrt{\frac{2}{\pi sr}} \ \mathrm{Im} \int_o^{\infty} H(t-t_A) \ pf(p) \ e^{-st} \ \frac{dp}{dt} dt \tag{2-18}$$

$$\frac{\partial \tilde{I}}{\partial z} = -s\sqrt{\frac{2}{\pi s r}}\ \mathrm{Im} \int_0^{\infty} H(t-t_A)\ \frac{\partial t}{\partial z}\ f(p) e^{-st}\ \frac{dp}{dt}\ dt \qquad (2\text{-}19)$$

The geometrical arrival time is defined by

$$\left.\begin{aligned} t_A &= t(r,z,p_o) \\ \frac{\partial t}{\partial p}\Big|_{p_o} &= 0 \end{aligned}\right\} \qquad (2\text{-}20)$$

If F(t) is the source function for the potentials, then the time domain equivalents to (2-18) and (2-19) are

$$\frac{\partial I(r,z,t)}{\partial r} = \frac{1}{\pi}\sqrt{\frac{2}{r}}\ \frac{\partial}{\partial t}\ \left\{F'(t) * \frac{H(t)}{t^{1/2}} * \mathrm{Im}\left(H(t-t_A) p f(p) \frac{dp}{dt}\right)\right\} \qquad (2\text{-}21)$$

$$\frac{\partial I(r,z,t)}{\partial z} = \frac{1}{\pi}\sqrt{\frac{2}{r}}\ \frac{\partial}{\partial t}\ \left\{F'(t) * \frac{H(t)}{t^{1/2}} * \mathrm{Im}\left(H(t-t_A) \frac{\partial t}{\partial z} f(p) \frac{dp}{dt}\right)\right\} \qquad (2\text{-}22)$$

where * indicates a convolution. To compute the first motion approximation we note that t(r,z,p) is of the form

$$t = pr + \eta_\alpha g_1(z) + \eta_\beta g_2(z) \qquad (2\text{-}23)$$

where $g_1(z)$ and $g_2(z)$ are listed in Table 1 for the various rays. Using the definition (2-20) and replacing t by t_A in the first motion approximation, we get

$$\frac{dp}{dt} \sim i\ \left[2(t-t_A)\left(\frac{g_1(z)}{\alpha^2 \eta_\alpha^3} + \frac{g_2(z)}{\beta^2 \eta_\beta^3}\right)\right]^{-1/2} \qquad (2\text{-}24)$$

so that, by substitution in (2-21) and (2-22), and reduction

$$\frac{\partial I(r,z,t)}{\partial r} \sim \frac{po\ f(po)\ F\ (t-t_A)}{\left[r\left(\frac{g_1(z)}{\alpha^2 \eta_\alpha^3(po)} + \frac{g_2(z)}{\beta^2 \eta_\beta^3(po)}\right)\right]^{1/2}} \qquad (2\text{-}25)$$

$$\frac{\partial I(r,z,t)}{\partial z} \sim \frac{1}{po}\ \frac{\partial t}{\partial z}\ \frac{\partial I}{\partial r} \qquad (2\text{-}26)$$

The displacement components for the various rays can be obtained by using these results in (2-1) and substituting the quantities from Table 1.

Table 1

Ray Description	$t(r,z,p)$	$\partial t/\partial z$	$f(p)$
INCIDENT P	$pr + \eta_\alpha \lvert z-h \rvert$	$\eta_\alpha \operatorname{sgn}(z-h)$	$p^{1/2}/\eta_\alpha$
REFLECTED P	$pr + \eta_\alpha (z+h)$	η_α	$4\mu^2(1-\Phi)\ p^{5/2}\ \eta_\beta/\mathcal{D}(p)$
TRANSMITTED P	$pr + \eta_\alpha (h-z)$	$-\eta_\alpha$	$2\mu\ \Phi p^{1/2}\ \eta_\beta/[\beta\eta_\alpha \mathcal{D}(p)] + (1-\Phi)p^{1/2}\ (\rho-2\mu p^2)^2/[\eta_\alpha \mathcal{D}(p)]$
REFLECTED S	$pr + \eta_\alpha h + \eta_\beta z$	η_β	$\mu\ (1-\Phi)\ p^{3/2}\ (2\mu p^2-\rho)/\mathcal{D}(p)$
TRANSMITTED S	$pr + \eta_\alpha h - \eta_\beta z$	$-\eta_\beta$	$\mu\ (1-\Phi)\ p^{3/2}\ (2\mu p^2-\rho)/\mathcal{D}(p)$

where $\mathcal{D}(p)$ is given by 2-13.

3. Radiation Patterns

Suppose the displacements found in the previous section are rotated to a coordinate system that renders the slipping interface vertical. For the purpose of our block motion study, such coordinates are Earth coordinates.

For a take-off angle of 90° in Earth coordinates all S radiation reflected from and transmitted through the interface is pure SH relative to the surface of the Earth. Displacement radiation patterns in that case are simple to understand and were computed for different values of the bonding parameter and the following values of the remaining parameters:

Parameter	Value
α/β	1.72
ρ	3.2 gms/cm^3
h	1.0 km
$R=[r^2+(z-h)^2]^{1/2}$	1000.0 km

Amplitudes are measured perpendicular and parallel to the ray joining the receiver and the source. This gives rise respectively to the transverse and radial components of displacement as seen in Fig. 3. The radiation patterns for a unit step source function are given in Fig. 4. where the solid and dotted lines are the transverse and radial components respectively, and where, positive for the transverse component is defined to be counter-clockwise. The horizontal axis represents the edge view of the slipping interface and the units on this axis

represent the ratio of the amplitude of the component to that of the incident P wave.

These patterns are seen to change shape with bonding. For $\phi = 0.0$ the angle of maximum displacement corresponds to angles of critical reflections. Similar lobed patterns were found by Burridge et al. (1964) for reflections from a free surface.

There is good conversion for bonding $\phi = 0.0$: the amplitude of the SH wave is at least 0.5 of the P wave. Conversion gets progressively smaller as the bonding is varied to higher values. For $\phi = 0.5$ and 0.9, the amplitude of the SH wave is, respectively, .1 and .01 of the P wave amplitude. This is due to the fact that as the bonding becomes stronger the jump in shear displacement across the interface decreases, and vanishes when the bonding is perfect, i.e., $\phi = 1.0$. This is seen in Fig. 5.

So it appears that a low value of the bonding parameter is needed for this mechanism to be an efficient shear wave generator. However these radiation patterns are subject to change in shape and amplitude with changes in the values of the parameters in the expressions for the displacement. Most important of these is the perpendicular distance h from the source to the slipping interface. As can be appreciated in the expressions for the displacements, 2-25 and 2-26, these vary as $h^{-1/2}$ in the high frequency, first motion approximation. Thus this linear theory predicts that if a slipping joint is sufficiently close to an underground explosion it could be an efficient converter of P to S waves. One must remember, however, that the approximation developed

in the previous section is far field and linear and therefore must break down for small h, so that this conclusion is only qualitative.

This faulting process due to the presence of a joint in the vicinity of an underground explosion gives rise to a different displacement pattern than that given either by the relief of prestress along a fault or the impinging of P waves on a slipless impedance mismatching surface, both of the same orientation as the joint. As appreciated in Fig. 4 the SH displacement radiation pattern has a cylindrical symmetry with respect to the line through the source and perpendicular to the interface: it is symmetric with respect to the interface but antisymmetric with respect to the line perpendicular to the interface through the source. The relief of prestress along a vertical fault, in this case, a vertical strike slip fault, has a double-couple radiation pattern which is symmetric with respect to the interface and the line perpendicular to the interface through the source as can be appreciated in Heaton (1979). On the other hand, the radiation pattern from the incidence of P waves on a slipless impedance mismatching surface has also cylindrical symmetry with respect to the line perpendicular to the interface and through the source but it differs from the radiation pattern of the slipping joint in that it is in general asymmetric with respect to the interface as is seen in Ewing et al. (1957).

This distinction of radiation patterns may provide the best tool through measurement to determine whether block motion is indeed a significant contributor of S waves from large underground explosions. It does not matter that the actual rheology of the fault is non-linear, for example Coulomb friction, because the radiation pattern of the first motion will have the same polarity as in this study. On the other hand

if the test site is significantly prestressed, observation of block motion through the polarity of the radiation pattern may be difficult to observe. Since Novaya Zemlya exhibits no seismicity, and this points to small, if any prestress, the records from underground explosions at that site would be those indicated to test this theory.

4. Summary and Conclusion

We have shown that a slipping interface separating identical materials give rise to conversion of P to S waves. This conversion is best when the materials are perfectly uncoupled and when the distance from the source to the interface is small. For these reasons, block motion may be an efficient generator of S waves from large underground explosions if cracks are quite near the source and/or the friction on the crack faces is small. To be able to determine whether this model is valid, one can make use of the displacement radiation patterns from tests in nuclear sites that exhibit no seismicity, as Novaya Zemlya.

5. Acknowledgements

The authors are grateful for many helpful critical comments and suggestions by members of the Seismological Laboratory and elsewhere, particularly those of C. B. Archambeau, L. Burdick, R. Butler, D. Harkrider, T. Heaton, D. Helmberger, G. Mellman and J. Rudnicki.

This research was conducted under a grant by the Advanced Research Projects Agency of the Department of Defense and monitored by the Air Force Office of Scientific Research under Contract No. A.F.O.S.R. F49620-77-C-0022. Contribution No. 3148, Division of Geological and Planetary Sciences, California Institute of Technology, Pasadena, California 91125.

References

Aki, K. and K. L. Larner (1970). Surface motion of a layered medium having an irregular interface due to an incident plane SH wave, J.G.R., 75, 933-954.

Aki, K., Tsai, Y. (1972) Mechanism of Love wave excitation by explosive sources, J. Geophys. Res., 77, 1452-1475.

Archambeau, C. B. (1972). The theory of stress wave radiation from explosions in prestressed media, Geophys. J. R. astr. Soc., 29, 329-366.

Archambeau, C. B. (1973). The theory of stress wave radiation from explosions in prestressed media, Appendix I, Geophys. J. R. astr. Soc., 31, 361-863.

Bache, T. C., D. G. Lambert (1976). The seismological evidence for the triggering of block motion by large explosions, Systems Science and Softwave Topical Reprint.

Burridge, R., E. R. Lapwood, L. Knopoff (1964). First motion from seismic sources near a free surface, B.S.S.A., 54, 1889-1913.

Cagniard, L. (1962). Reflection and Refraction of Progressive Seismic Waves. Translated by E. A. Flinn and C. H. Dix. McGraw Hill Book Co., Inc.

Chez, E. L., J. Dundurs and M. Comninou (1978). Reflection and refraction of SH waves in presence of slip and friction, B.S.S.A., 68, 999-1012.

de Hoop, A. T. (1960). A modification of Cagniard's method for solving seismic seismic pulse problems, Appl. Sci. Res., 8, 349-356.

Ewing, W. M., Jardetaky , W. S., F. Press (1957). Elastic Waves in Layered Media, McGraw Hill Book Co., Inc.

Heaton, T. H. (1979). Generalized ray models of strong ground motion. Ph.D. Thesis, California Institute of Technology

Helmberger, D. V. (1974). Generalized ray theory for shear dislocations, B.S.S.A., 64, 45-64.

Kanai, K. (1961). A new problem concerning surface waves, Bull. Earthquake Res. Inst., 39, 359-366.

Kisslinger, C., E. J. Mateker, T. V. McEvilly (1961). SH motion from explosions in soil, J. Geophys. Res., 66, 3487-3496.

Langston, C. A. (1976). Body wave synthesis for shallow earthquake sources: Inversion for source and Earth structure parameters, Ph.D. thesis, California Institute of Technology.

Miller, R. K. (1979). An estimate of the properties of Love-type surface waves in a frictionally bonded layer, B.S.S.A., 69, 305- .

Murty, G. S. (1975). A theoretical model for the attenuation and dispersion of Stoneley waves at the loosely bonded interface of elastic half-spaces, Phys. Earth Planet. Int., 11, 65-79.

Murty, G. S.(1976). Reflection, transmission and attenuation of elastic waves at a loosely-bonded interface of two half spaces, Geophys. J. R. astr. Soc., 44, 389-404.

Salvado, C. A. and J. B. Minster (1977). Compressional waves incident on a loosely bounded interface of two identical solids, EOS (Am. Geophys. U. Trans.), 58, 1193.

Sezawa, K. and K. Kanai (1940). A fault surface or a block absorbs seismic wave energy. Bull. Earthquake Res. Inst., 18, 465-482.

Figure Captions

Figure 1. A purely dilatational point source is located at a height h above the slipping interface separating identical half-spaces.

Figure 2. The identical half-spaces are separated by an interface which is assumed a fluid filled gap of viscosity η.

Figure 3. Amplitudes are measured perpendicular (transverse component T) and parallel (radial component R) to the ray joining source with receiver.

Figure 4. Radiation patterns for a take-off angle of 90°. Solid line represents the transverse component while the dotted line represents the radial component.

Figure 5. Displacement jump across the slipping interface for various values of bonding parameter ϕ.

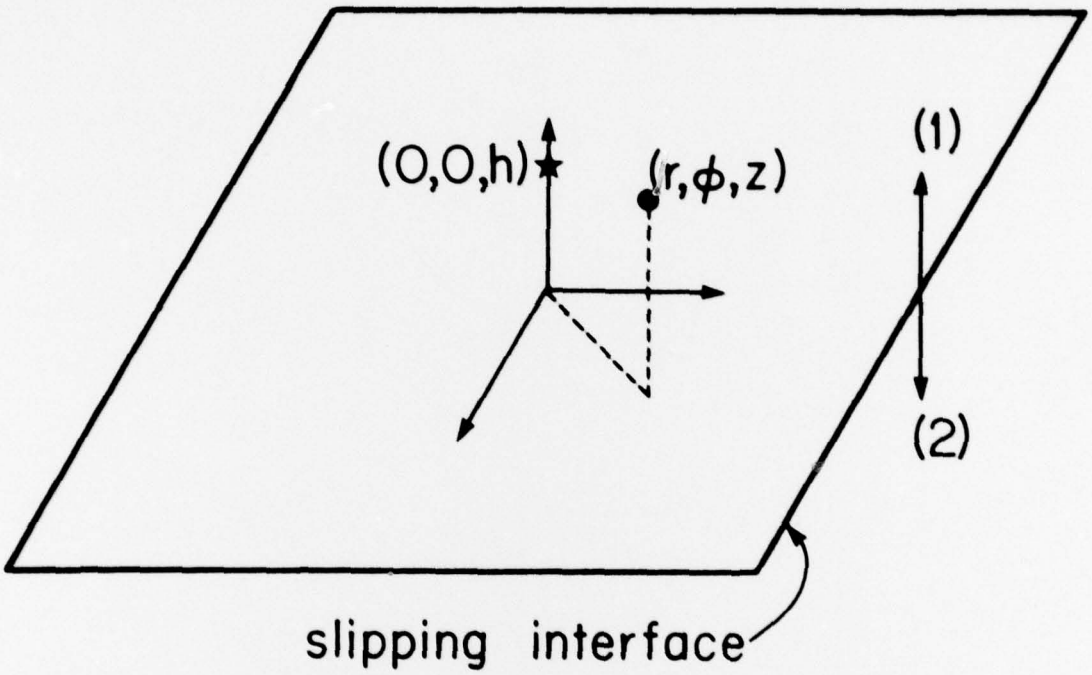

Fig. 1

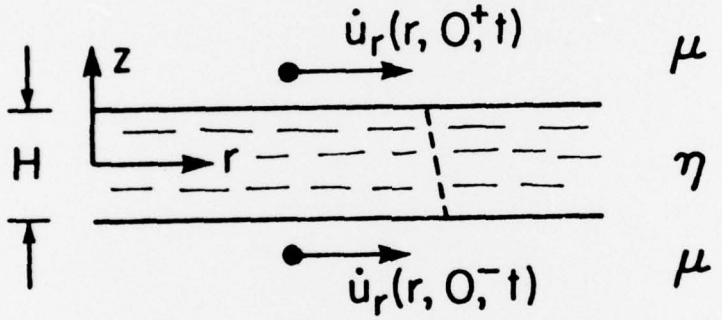

Fig. 2

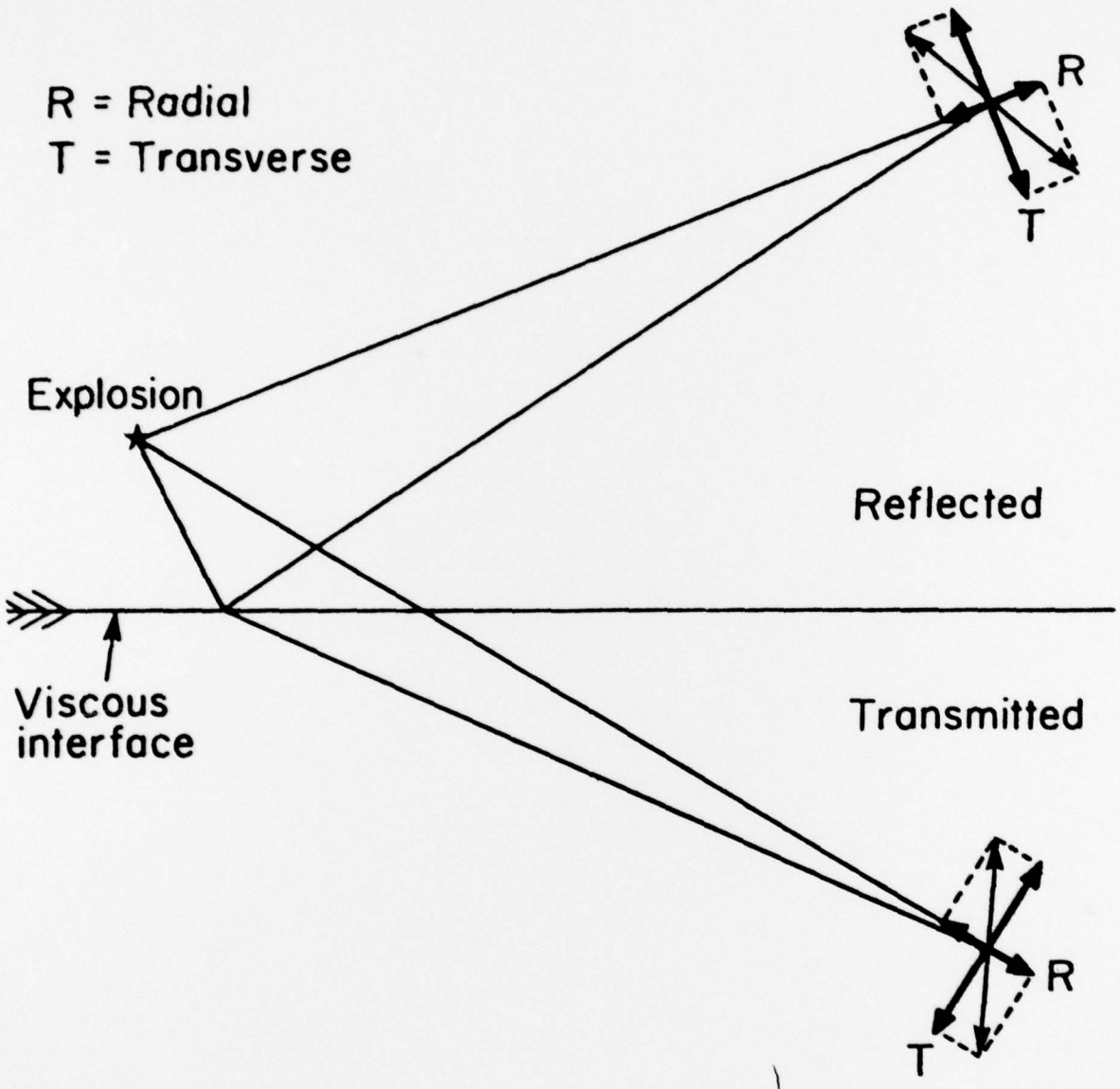
R = Radial
T = Transverse
R
T
Explosion
Reflected
Viscous
interface
Transmitted
R
T

Fig. 3

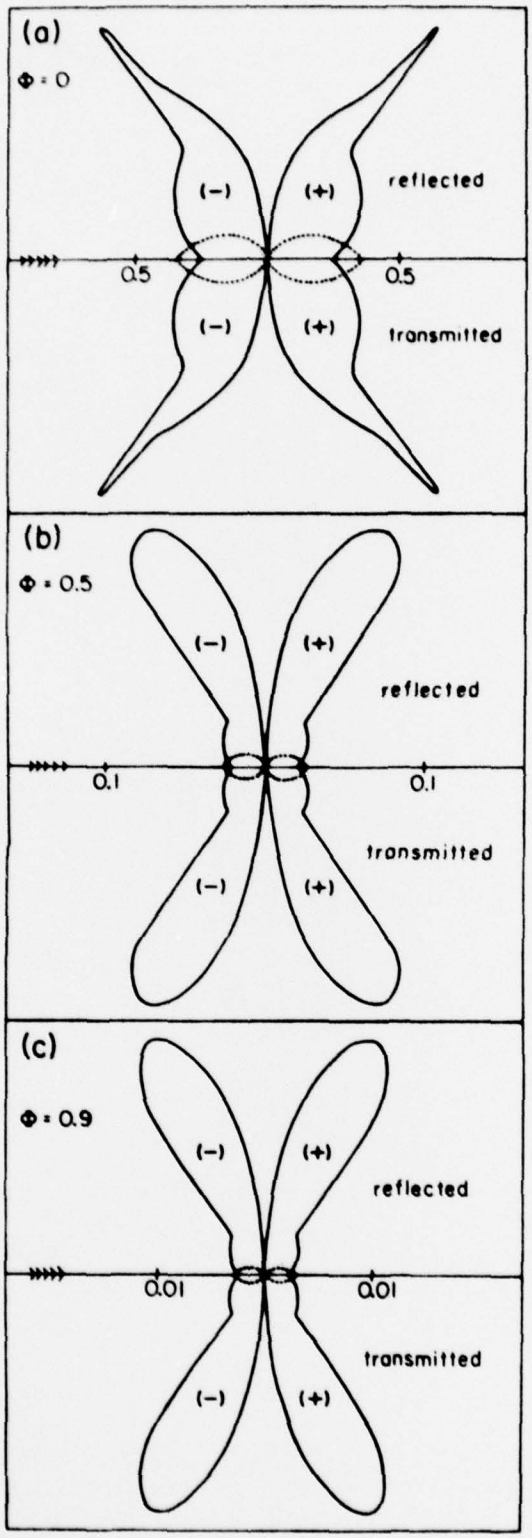
(a)
Φ = 0
(−)
(+)
reflected
0.5
0.5
(−)
(+)
transmitted
(b)
Φ = 0.5
(−)
(+)
reflected
0.1
0.1
transmitted
(−)
(+)
(c)
Φ = 0.9
(−)
(+)
reflected
0.01
0.01
transmitted
(−)
(+)

Fig. 4

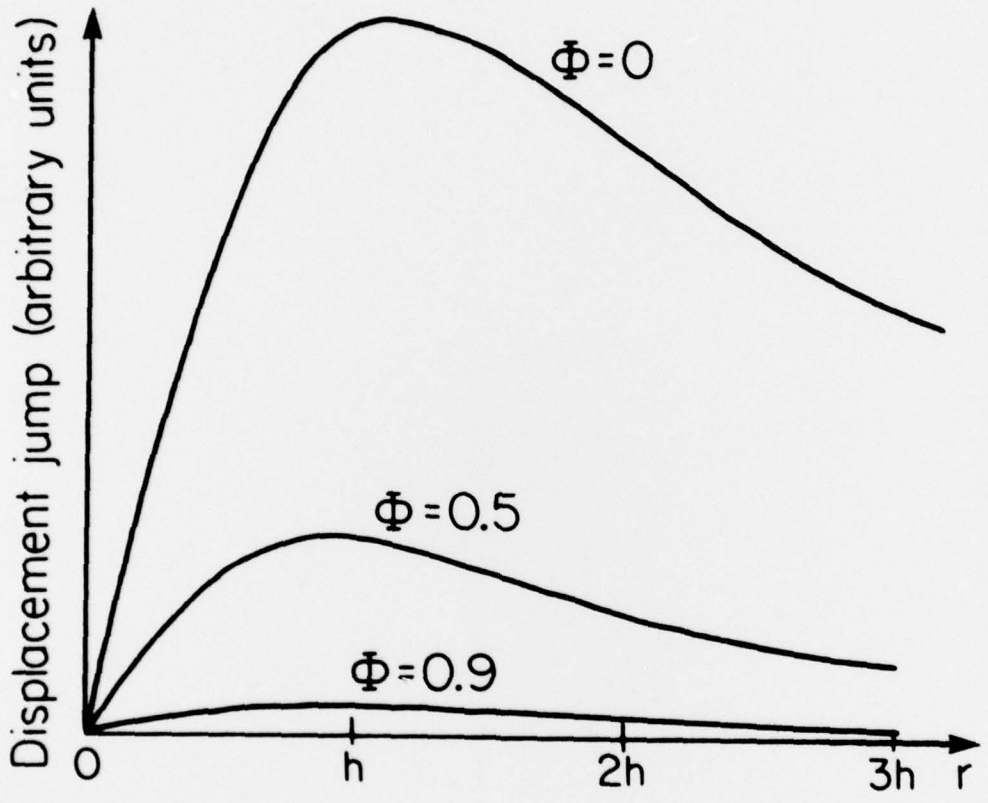

Fig. 5